UCLA
UCLA Previously Published Works

Title

Dual Knockout Models of the Spatially and Functionally Conserved rgra and rgrb Zebrafish Genes Reveal the Requirement of RGR for the Integrity of Cone-Mediated Photopic Vision, the Photopic Visual Cycle and Bruch's Membrane Morphology

Permalink

https://escholarship.org/uc/item/1dw233qz

Journal

The FASEB Journal, 40(10)

ISSN

0892-6638

Authors

Ruddin, Grace
McCann, Tess
Kaylor, Joanna J
et al.

Publication Date

2026-05-31

DOI

10.1096/fj.202504935r

Copyright Information

This work is made available under the terms of a Creative Commons Attribution-NonCommercial License, available at https://creativecommons.org/licenses/by-nc/4.0/

Peer reviewed

eScholarship.org Powered by the California Digital Library
University of California

Check for updates

The FASEB Journal

FASEB
Federation of American Societies for Experimental Biology

RESEARCH ARTICLE OPEN ACCESS

Dual Knockout Models of the Spatially and Functionally Conserved *rgra* and *rgrb* Zebrafish Genes Reveal the Requirement of RGR for the Integrity of Cone-Mediated Photopic Vision, the Photopic Visual Cycle and Bruch's Membrane Morphology

Grace Ruddin[1,2] | Tess McCann[1,2] | Joanna J. Kaylor[3] | Michelle M. Fox[1,4] | John D. Fehilly[1,2] | Rebecca Ward[1,2] | Adam Faulkner[1,2] | Ailís L. Moran[1,2] | Kieran Wynne[5] | Roxana A. Radu[3] | Michael G. Monaghan[6,7] | Stephen D. Thorpe[1,4,7] | Gabriel H. Travis[3,8] | Breandán N. Kennedy[1,2]

[1]University College Dublin Conway Institute of Biomolecular and Biomedical Research, University College Dublin, Dublin 4, Ireland | [2]University College Dublin School of Biomolecular and Biomedical Science, University College Dublin, Dublin 4, Ireland | [3]UCLA Stein Eye Institute, Department of Ophthalmology, University of California Los Angeles David Geffen School of Medicine, Los Angeles, California, USA | [4]University College Dublin School of Medicine, University College Dublin, Dublin, Ireland | [5]Systems Biology Ireland, University College Dublin, Dublin, Ireland | [6]Discipline of Mechanical, Manufacturing and Biomedical Engineering, School of Engineering, Trinity College Dublin, Dublin, Ireland | [7]Trinity Centre for Biomedical Engineering, Trinity College Dublin, Dublin, Ireland | [8]University of California Los Angeles, Department of Biological Chemistry, Los Angeles, California, USA

Correspondence: Breandán N. Kennedy (brendan.kennedy@ucd.ie)

Received: 19 December 2025 | **Revised:** 8 April 2026 | **Accepted:** 28 April 2026

Keywords: Bruch's membrane | Photoisomerase | retinoids | RGR | vision | zebrafish

ABSTRACT

The retinal G protein-coupled receptor (RGR) is a visual cycle photoisomerase that photopically regenerates 11-*cis*-retinal (11cRAL). It plays a crucial role in sustaining vision. Here, we investigated the in vivo role of RGR in the cone photoreceptor-dominant, zebrafish retina, focusing predominantly on how visual function is impacted in the absence of RGR. There are two zebrafish *RGR* paralogs, *rgra* and *rgrb,* both with predominant expression in retinal pigment epithelium (RPE) and Müller glia cells. Under standard light rearing conditions, bespoke *rgrb*$^{-/-}$; *rgra*$^{-/-}$ double knockout zebrafish present with a ~21% reduction in optokinetic response (OKR) saccades per minute relative to wild-type (WT). This impaired visual behavior worsens in higher photopic conditions ranging from 20 000–81 000 lx. In contrast, no significant OKR defect is observed under dark-adapted conditions, consolidating the light-dependent role of RGR in vision. Retinoid profiling of *rgrb*$^{-/-}$; *rgra*$^{-/-}$ zebrafish larvae demonstrated significant decreases in 11cRAL levels under standard and brighter light rearing conditions. Proteomic profiling validated the successful generation of *rgrb*$^{-/-}$; *rgra*$^{-/-}$ zebrafish and revealed an unanticipated upregulation in ocular extracellular matrix proteins. From polarized light microscopy, increased collagen fiber abundance with dysregulated organization in Bruch's membrane at the interface between the retina and choroid was observed. These novel findings demonstrate the role of RGR in sustaining visual function under cone-mediated photopic conditions, a concomitant deficit in the photopic visual cycle and a novel role in maintaining the integrity of Bruch's membrane.

Abbreviations: 11cRAL, 11-*cis*-retinal; AMD, Age-related macular degeneration; atRAL, all-*trans*-retinal; atROL, all-*trans*-retinol; atRP, all-*trans*-retinyl palmitate; Bp, Base pairs; Dpf, Days post fertilization; ECM, Extracellular matrix; Hpf, Hours post fertilization; IRD, Inherited retinal degeneration; RGR, Retinal G Protein-Coupled Receptor (generic); RGR, Retinal G Protein-Coupled Receptor (protein human); Rgra, Retinal G Protein-Coupled Receptor (protein zebrafish); Rgrb, Retinal G Protein-Coupled Receptor (protein zebrafish); *RGR*, Retinal G Protein-Coupled Receptor (gene human); *rgra*, Retinal G Protein-Coupled Receptor (gene zebrafish); *rgrb*, Retinal G Protein-Coupled Receptor (gene zebrafish); OKR, Optokinetic Response; RPE, Retinal pigment epithelium; spm, Saccades per minute; WT, Wild-type.

This is an open access article under the terms of the Creative Commons Attribution-NonCommercial License, which permits use, distribution and reproduction in any medium, provided the original work is properly cited and is not used for commercial purposes.

© 2026 The Author(s). *The FASEB Journal* published by Wiley Periodicals LLC on behalf of Federation of American Societies for Experimental Biology.

1 | Introduction

The visual chromophore, 11-*cis*-retinal (11cRAL), a light-sensitive aldehyde form of vitamin A, is needed for phototransduction and therefore its regeneration is fundamental to maintaining vision. The 11-*cis* to all-*trans* isomerisation of visual chromophores during phototransduction needs to be reversed for vision to be maintained [1]. Vitamin A is predominantly stored in the retinal pigment epithelium (RPE) layer of the outer retina, with photoreceptors using the active chromophore 11cRAL in visual pigments for phototransduction [1]. Cone photoreceptors are critical for color detection and to sense photons in ambient or bright light. Therefore, cone photoreceptors are required for photopic vision, the process of mediating vision in bright light conditions. The canonical visual cycle, driven by the isomerase RPE65, uses retinyl esters to regenerate 11cRAL but is insufficient under photopic conditions [1, 2]. One proposed mediator of an alternative visual cycle that regenerates 11cRAL under photopic conditions is the retinal G protein-coupled receptor (RGR). RGR belongs to the opsin GPCR family, specifically the retinal photoisomerase subfamily, along with retinochrome [3]. Orthologues of RGR are conserved across many species, including humans, cows [4], mice [5], and chickens [6], but not in the genomes of marsupials [7, 8]. RGR is a seven-transmembrane protein predominantly expressed in the RPE and Müller glia cells of the retina [9–12].

Eye diseases associated with mutations in RGR include inherited retinal degeneration (IRD) and age-related macular degeneration (AMD). There is currently only one confirmed pathogenic RGR variant associated with IRD, with individuals having a range of retinal changes [13, 14]. For example, non-invasive imaging indicated some individuals with loss of outer retinal layers [14] or reduced electroretinogram amplitudes [13, 14]. In AMD, a major clinical hallmark is the buildup of drusen between the RPE and Bruch's membrane. Notably, an RGR splice variant, RGR-d [15], localizes predominantly at the basal side of RPE cells [16], with deposits reported in Bruch's membrane [17, 18].

RGR is a non-visual opsin. Instead, in the retina, it acts as a visual cycle photoisomerase [10–12, 19–22], binding all-*trans*-retinal (atRAL) [4, 19, 23, 24] to generate 11cRAL in the presence of light. The Schiff base linkage at a conserved lysine residue in RGR mediates substrate binding of atRAL [11]. In addition to photogenerating 11cRAL, under light and dark conditions, RGR is also reported to regulate the levels of retinyl esters [20, 25]. In the presence of light, all-*trans*-retinyl esters (atRE) significantly increased in *Rgr* knockout mice [20]. Under dark conditions, RGR inhibits lecithin retinol acyltransferase (LRAT) and all-*trans*-retinyl ester hydrolase activities [25]. RGR is reported to mediate the movement of atRE from lipid droplet storage pools to isomerase pools in the endoplasmic reticulum [25].

To date, no studies have investigated the biological role of RGR using an in vivo cone-dominant model, nor have they reported on the impact on functional vision of *RGR* knockouts. The zebrafish is a vertebrate model organism, excellent for studying vision [26]. The zebrafish retina is cone-dominant, correlating with diurnal behavior [26]. Due to a whole-genome duplication event, zebrafish often display two orthologs of mammalian genes [26]. There are two *RGR* paralogs in zebrafish: *rgra* and *rgrb*. The zebrafish eye develops rapidly, with a functional visual system apparent by 5 days post-fertilization (dpf) [27]. Thus, functional vision assays in zebrafish larvae under standard, dark and photopic conditions are amenable. This study investigated the role of *rgra* and *rgrb* in visual biology using CRISPR-Cas9-generated double knockout $rgrb^{-/-}$; $rgra^{-/-}$ zebrafish.

The levels of light and wavelengths of light needed for RGR photoisomerisation activity show context-dependent variations [2]. For example, a significant reduction in total retinal levels was observed when $Rgr^{-/-}$ mice were exposed to 4000 lx for 8 h, or 1400 or 14 000 lx for 10 h compared to $Rgr^{+/+}$ [20]. In vitro, bovine RGR maximally photogenerates 11cRAL at 530 nm light [11, 12, 22].

Our aim was to report on visual behavior phenotypes of $rgrb^{-/-}$; $rgra^{-/-}$ zebrafish under photopic conditions. We investigated whether the loss of both *rgra* and *rgrb* paralogs would selectively result in reduced visual function under photopic conditions. We hypothesized that a decrease in visual function would correlate with decreased 11cRAL levels. We undertook proteomic profiling to validate the generation of the zebrafish $rgrb^{-/-}$; $rgra^{-/-}$ double knockouts and to determine what proteins would be dysregulated in the absence of Rgra and Rgrb. Finally, we determined whether retinal morphology, particularly Bruch's membrane, would be disrupted in the absence of *rgra* and *rgrb*. In summary, using the zebrafish model, we demonstrated the role of RGR in sustaining cone-based vision under photopic conditions through its role in photogenerating the visual chromophore.

2 | Methods

2.1 | Zebrafish Maintenance and Husbandry

Zebrafish embryos produced by natural spawning and larvae up to 131 hpf were raised in an incubator under a 14:10 h light: dark cycle at 27°C in 10 cm Petri dishes of E2 embryo medium (0.137 M NaCl, 5.4 mM KCl, 5.5 mM Na_2HPO_4, 0.44 mM KH_2PO_4, 1.3 mM $CaCl_2$, 1.0 mM $MgSO_4$, and 4.2 mM $NaHCO_3$, conductivity ~1400–1600 μS, pH ~ 7) containing methylene blue, unless stated otherwise. Juvenile and adult zebrafish were housed in 1–10 L tanks in a recirculating Aquatic Habitats water system at 28°C under a 14:10 h light: dark cycle. Until 28 dpf, juvenile zebrafish were gradually introduced to the main diet of pellet food (Gemma micro, Skretting) and brine shrimp (Artemia sp.). Adult zebrafish were fed pellet food twice daily (once daily on weekends) and brine shrimp once daily.

2.2 | Ethics Statement

All experiments involving zebrafish were conducted at the UCD Zebrafish facility in accordance with ethical approvals and exemptions granted by the Animal Research Ethics Committee (AREC-20-10-KENNEDY, AREC-E-20-15-KENNEDY) and project authorisations from the Health Products Regulatory Authority (Project Authorisation AE18982/P186).

15306860, 2026, 10, Downloaded from https://faseb.onlinelibrary.wiley.com/doi/10.1096/fj.202504935R by University Of California, Los Angeles, Wiley Online Library on [17/06/2026]. See the Terms and Conditions (https://onlinelibrary.wiley.com/terms-and-conditions) on Wiley Online Library for rules of use; OA articles are governed by the applicable Creative Commons License

2.3 | Analysis of Zebrafish *Rgra* and *Rgrb* Expression and Conservation

Orthologs of *Rgr* were identified using the Alliance of Genome Resources. Protein sequences for human, mouse, and zebrafish Rgr orthologs were retrieved from UniProt (uniprot.org). For phylogenetic analysis, the Seaview package (version 5.04) [28] was used to construct a Clustal Omega multiple sequence alignment [29] of representative zebrafish and human non-visual opsin proteins, and to infer a phylogenetic tree using Maximum Likelihood (PhyML, LG substitution model) [30], with 100 bootstrap replicates. These sequences were aligned using the Clustal Omega multiple sequence alignment tool. The resulting alignment was visualized in Jalview (https://jalview.org) and colored according to percentage identity. Conserved residues were manually annotated.

The publicly available resource Daniocell (https://daniocell.nichd.nih.gov), which depicts the gene expression data from embryonic or larval wild-type (WT) (TL/AB) zebrafish, was used to generate *rgra* and *rgrb* expression patterns and respective developmental time courses. Data from this resource is from previously published work [31]. Analysis of single cell RNA-sequencing (scRNA-seq) from adult zebrafish was obtained from previously published work [32] using the online webtool (https://viz.stjude.cloud) to generate *rgra* and *rgrb* gene expression clustering patterns and heatmaps.

2.4 | Generation of *rgra*, *rgrb* and *rgrb*$^{-/-}$; *rgra*$^{-/-}$ Zebrafish

To establish zebrafish germline knockouts of *rgra*, two CRISPR guides (5′-*GTGGAGCAGTGCCATCACCC*-3, 5′-*CAATAACGGTGACAGCGTTC*-3′) were microinjected into one-cell stage zebrafish embryos, which targeted exons 4 and 2, respectively. The creation of a 2209 base pair (bp) deletion was validated by Sanger sequencing. To generate knockouts of *rgrb*, two CRISPR guides (5′-*CCTCAACATCAACGGCCTAG*-3′, 5′-*TCTGGATCCTGGCTGTGTTC*-3′) targeting exons 2 and 4, respectively, resulted in a 341 bp deletion, which was validated by Sanger sequencing. Injected larvae raised to adulthood were outcrossed to screen for germline transmission of the null target gene. Homozygous F2 mutants were generated by incrossing isogenic F1 heterozygous adult fish, which were initially generated by outcrossing a founder fish. The inclusion of *rgra* and *rgrb* knockout lines generated the *rgrb*$^{-/-}$; *rgra*$^{-/-}$ double knockout lines.

2.5 | Genotyping Zebrafish Larvae and Adults

DNA was extracted from either whole 5 dpf zebrafish larvae or a section of an adult caudal fin using 50 μL lysis buffer (10 mM Tris–HCl, 50 mM KCl, 0.3% NP40, 0.3% Tween, pH 8.3) and 1:50 Proteinase K. Samples were incubated at 55°C overnight before the Proteinase K was inactivated at 95°C for 15 min. The supernatant was used as a genomic DNA template in a 25 μL polymerase chain reaction (PCR) consisting of primers (Table 1), Dream Taq enzyme and nuclease-free water. The PCR cycling conditions used for *rgra* were 3 min at 95°C, 35 cycles of 30 s at 95°C, 30 s at 60°C, 1 min at 72°C, and a final elongation of 72°C for 5 min. The PCR cycling conditions used for *rgrb* were 3 min at 95°C, 33 cycles of 30 s at 95°C, 30 s at 57.6°C, 1 min at 72°C, and a final elongation of 72°C for 5 min. PCR products were run on a 1% agarose gel stained with SYBR safe DNA gel stain and compared against a 100 bp DNA ladder (Invitrogen). The *rgra*$^{+/+}$ and *rgrb*$^{+/+}$ band sizes measure 584 bp and 586 bp, respectively, with the *rgra*$^{-/-}$ and *rgrb*$^{-/-}$ band sizes measuring 412 bp and 245 bp, respectively.

TABLE 1 | List of PCR primers used for genotyping zebrafish larvae and adults.

Primer Name	Sequence 5′-3′
rgra forward	TTCGATGTGTTTTCCCTCGGAT
rgra reverse	CACCCTTGCTATAGTCCAGTGT
rgra poison	CCTCTTACCTAACAGCTGCACT
rgrb forward	ATCAGCCTCTACAGCTGC
rgrb reverse	GCTCGAAGTCGAACACAC

2.6 | Quantitative PCR

For quantitative PCR experiments, 5 dpf larvae were collected in tubes containing 10–20 larvae per tube and stored in RNALater (Sigma). The pools of whole larvae were homogenized through a 26-gauge needle/syringe, and total RNA was extracted using TRIzol (ThermoFisher Scientific). RNA was precipitated with phenol-chloroform and resuspended in nuclease-free water. The total RNA concentration and integrity (260/280) were quantified using the DeNovix DS-11 Series Spectrophotometer, and samples were stored at −80°C to prevent degradation until further use. RNA was treated with DNase (AMPD1, Sigma-Aldrich). cDNA was synthesized from 500 ng of total RNA using the PrimeScript RT reagent kit (Perfect Real Time, TAKARA, Japan). Quantitative real-time PCRs were carried out using a QuantStudio 7 Flex Real-Time PCR System (Applied Biosystems). Targets were detected using PowerSYBR Green PCR Master Mix (Applied Biosystems) under the following conditions: 50°C for 2 min, 95°C for 10 min, then 40 cycles at 95°C for 15 s and 60°C for 60 s. Results were analyzed using Quantstudio Real-time PCR software. All reactions were performed in technical triplicate. Relative expression of targets was assessed by the $2^{-\Delta\Delta CT}$ method using β-actin as the housekeeping gene. Primers that spanned across exons for each target gene were designed using Primer3. Primer sequences are shown in Table 2.

2.7 | Zebrafish Optokinetic Response (OKR)

Zebrafish larvae were raised under different conditions prior to OKR analysis. Standard rearing conditions involved raising larvae in a 27°C incubator under a 14:10 h light (~450 lx): dark cycle, with OKR analysis occurring at ~124–126 hpf. "Dark-adapted" larvae were raised under similar conditions except they remained in the dark from 120 hpf until OKR analysis

15306860, 2026, 10, Downloaded from https://faseb.onlinelibrary.wiley.com/doi/10.1096/fj.202504935R by University Of California, Los Angeles, Wiley Online Library on [17/06/2026]. See the Terms and Conditions (https://onlinelibrary.wiley.com/terms-and-conditions) on Wiley Online Library for rules of use; OA articles are governed by the applicable Creative Commons License

TABLE 2 | List of primers used for quantitative PCR.

Gene	Forward	Reverse
rgra	CCTCTGTTTGGTTGGGGAGA	AAGACAGCACCACAAACACC
rgrb	GGCTTCACCGACTTCGACAT	CGTCTGCATCTCTCGAACCC
actb1	CTTCCTGGGTATGGAATCTTGC	GTGGAAGGAGCAAGAGAGGTG

at ~124.5–126 hpf. Larvae, which were raised under increased levels of light for 6 h, were raised under standard conditions until 120 hpf. They were raised in a wooden box lined with aluminium foil and exposed to either 40-50 K lx at 100% power or 20-25 K lx at 50% power from a Schott KL 2500 LED light source until ~126 hpf. Larvae which underwent the 8-h light treatment were raised under standard conditions until 120 hpf. They were then transferred to a 60 mm dish and placed in a mating tank lined with aluminium foil inside a cardboard box. Larvae were exposed to a light intensity of 81 K lx from a Schott KL 2500 LED light source at 100% power until ~128.5 hpf. OKR assays were conducted between 12 to 3 pm (standard, dark-adapted and 6-h bright light rearing) to ensure data consistency [33] or between 4 pm–6.45 pm (8-h bright light rearing). For the OKR assay, the larvae dish is placed on a table under ambient light room conditions (571 lx), and the visual behavior of the larvae is assessed one by one. Larvae are immobilized in the centre of a 60 mm Petri dish containing prewarmed 9% methylcellulose (viscosity: 25 cP, Sigma) solution in E2 embryo media. A "standard OKR assay" in our case refers to a 3D printed drum with black and white stripes spaced at 0.02 cycles per degree rotating at 19 rotations per minute; 30 s in a clockwise direction, and 30 s in an anticlockwise direction under a light intensity of 30 233 lx from a Schott KL 2500 LED light source at 22.7% power. Performing the OKR and quantifying the saccadic responses was based on a previous publication [33]. In some cases, light measurements are the average of triplicate values recorded with a Sauter SO 200 K lx meter.

2.8 | Retinoid Profiling Analysis

Analysis of zebrafish larvae retinoid levels was conducted on 51 zebrafish larvae (< 131 hpf) per strain, per replicate, as previously described [34], with analysis of adult zebrafish conducted as previously described [35]. Larval and adult zebrafish were euthanized in tricaine (MS-222) before being collected under dim red light or prior to enucleation of both eyes under dim red light, respectively. All samples were snap frozen in liquid nitrogen and stored at −80°C. Retinoid extractions were conducted under dim red light in a dark room for normal phase high-performance liquid chromatography (HPLC) analysis of retinoids. The individual biological replicates were stored at −80°C and thawed on ice before being homogenized in 500 μL phosphate-buffered saline (PBS) using a glass tissue grinder (Kontes). 50 μL of the homogenate was taken to determine the protein concentration using a Micro BCA protein assay kit (Pierce), with 25 μL of 5% Sodium Dodecyl Sulfate (SDS) (~0.2% SDS final concentration) and 50 μL of brine added to the remaining 450 μL sample. The samples were briefly mixed. To generate retinal oxides, hydroxylamine hydrochloride (500 μL of 1.0 M solution in pH 7.0 PBS) was added. The samples were vortexed and incubated at room temperature for 15 min. 2 mL of cold methanol was added for the aqueous phase, which quenched and diluted the sample. 2 mL of hexane was added to extract the samples on two occasions, with brief vortexing and centrifugation at 3000 g for 5 min used to separate the phases between additions. Pooled hexane extracts were added to 13 x 100 mm borosilicate test tubes and evaporated under a stream of nitrogen. 100 μL hexane was added to dissolve the dried samples, which were then analyzed by normal HPLC using an Agilent 1100 series chromatograph equipped with a Supelcosil LC-Si column (4.6 x 250 mm, 5 μm). A 0.2%–10% dioxane gradient of hexane at a flow rate of 2 mL per minute was used. A photodiode-array detector was used to analyze the eluted mobile phase. For all eluted peaks, spectra (210–450 nm) were acquired. By comparing the spectra and the elution times of known authentic retinoid standards, the identification of the eluted peaks was established. Retinoid amounts were quantified by comparison with their respective peak areas to calibration curves established with retinoid standards.

2.9 | Immunofluorescence Imaging

Zebrafish larvae < 131 hpf were fixed overnight in 4% paraformaldehyde (PFA; Sigma) in PBS. Fixed larvae were then incubated in 25% sucrose (Sigma) in PBS for 24 h or until they had sunk, followed by incubation in 35% sucrose in PBS for 24 h or until submerged. Larvae were embedded in OCT compound and frozen, and 25 μm cryosections were collected using a Leica CM1860 UV cryostat and mounted onto Epredia Superfrost Plus Adhesion microscope slides. Sections were post-fixed for 15 min in 4% PFA in PBS, washed in PBSDT (PBS with 0.1% Tween-20 and 1% DMSO), and blocked for 1 h in PBSDT containing 5% normal goat serum (Sigma). Slides were incubated overnight at 4°C with the following primary antibodies: zpr1 (1:200; ZIRC; RRID:AB_10013803; cone cytoplasm) and peripherin-2 (1:100; Proteintech #18109–1-AP; RRID:AB_10665364). After washing, sections were incubated with secondary antibodies (1:500; Alexa Fluor 647 anti-rabbit and Alexa Fluor 488 anti-mouse; Cell Signaling Technology). Nuclei were counterstained with Hoechst 33342 (1:1000). Following final washes, sections were mounted with Aqua-Poly/Mount (Polysciences) and coverslipped. Images were acquired using a Zeiss LSM 800 Airyscan confocal microscope with 20× and 63× objectives. All images shown include the optic nerve and represent maximal frontal orthogonal projections.

2.10 | Histological Analysis

Zebrafish larvae < 131 hpf were euthanised in tricaine (MS-222) and fixed in glass vials containing 2% PFA and 2.5%

15306860, 2026, 10, Downloaded from https://faseb.onlinelibrary.wiley.com/doi/10.1096/fj.202504935R by University Of California, Los Angeles, Wiley Online Library on [17/06/2026]. See the Terms and Conditions (https://onlinelibrary.wiley.com/terms-and-conditions) on Wiley Online Library for rules of use; OA articles are governed by the applicable Creative Commons License

glutaraldehyde in 0.1 M Sorenson's phosphate buffer (pH 7.3) fixative solution at 4°C for 1–2 days. Samples were washed in 0.1 M Sorenson's phosphate buffer before post-fixation in 1% osmium tetroxide. Samples were dehydrated using a series of ethanol gradient concentrations (30%, 50%, 70%, 90%, 100%). Prior to the samples being incubated in Epon 812 resin overnight, the samples were incubated with propylene oxide. The samples were fixed in fresh resin overnight at 60°C. The resin blocks were cut into 1000 nm thick sections using a Leica ultramicrotome EM UC6 and stained with toluidine blue.

2.11 | Proteomic Profiling

Proteomic profiling was conducted as previously described [34].

2.11.1 | Sample Preparation

Eyes from adult zebrafish (four biological replicates per genotype) were dissected and stored at −80°C before tissue pellets were resuspended in 50 μL of ice-cold 8 M urea/50 mM Tris–HCL with phosphatase and protease inhibitors (Roche). A Branson Sonifier sonicated the samples three times for 10 s at 10% power, and protein concentrations were measured using a Nanodrop (Denovix). 200 μg of protein was carried forward for digestion. 8 mM dithiothreitol (DTT) reduced the protein samples, which were incubated at 1200 rpm for 30 min at 30°C. Alkylation was performed with the addition of 20 mM iodoacetamide and incubation under the same conditions for 30 min in the dark. With a Thermo Fisher Scientific KingFisher Flex using a high-throughput semi-automated label-free trypsin digestion protocol developed at the Novo Nordisk Foundation Center for Protein Research [36], the samples were trypsin digested.

2.11.2 | Mass Spectrometry

Using a Bruker timsTof Pro mass spectrometer connected to an Evosep One liquid chromatography system, 1 μg of pooled sample was analyzed. Tryptic peptides were resuspended in 0.1% formic acid and loaded onto an Evosep tip, with the Evosep being configured to pick up each tip, elute, and separate the peptides using a set chromatography method (30 samples a day) [37]. The mass spectrometer was operated in positive ion mode with a capillary voltage of 1300–1600 V, dry gas flow of 3 L/min, and a dry temperature of 180°C, with data being acquired with the instrument operating in a data dependent analysis parallel accumulation serial fragmentation mode (dda-PASEF). Using parallel accumulation serial fragmentation (PASEF), trapped ions were selected for ms/ms. A scan range of (100–1700 m/z) was performed at a rate of 4 PASEF MS/MS frames to 1 MS scan with a cycle time of 0.53 s [38]. The resultant file was used to create the data independent analysis parallel accumulation serial fragmentation (dia-PASEF) method within Bruker timsControl software. The scan mode dia-PASEF was selected. The pooled sample dda-PASEF file was opened in the window editor in the MS/MS tab. Once opened, the adjustable rhomboid was used to select the area of the heat map where the identifiable peptides (central region in the heat map containing peptides with charge states from + 2 to + 5) can be located. To summarize, the dia-PASEF settings used were mass width 26.0 Da, mass overlap 1.0, mass steps per cycle 35, mobility overlap 0.00, mass range 325.2–1201.2 m/z. All samples were acquired using dia-PASEF [39].

2.11.3 | Data Analysis

Using DIA-NN 2.1.0 Academia (Data-Independent Acquisition by Neural Networks), data acquired using dia-PASEF were analyzed [40]. The *Danio rerio* subset from The Uniprot Swissprot/Trembl database was used to create a spectral library within DIA-NN (library free mode). Specific search settings included cysteine carbamidomethylation enabled as a fixed modification, maximum missed cleavages 1, min precursor + 2, max precursor + 4, neural network (cross validated) was used. Cross-run normalization was set to retention time dependent, and library generation was set to ID's, RT & IM profiling. Precursor FDR was set to 1%. The Perseus computational platform (version 2.1.3.0) was used to process MaxQuant results [41]. To examine changes in protein expression using volcano plots, data were log transformed, missing values were imputed with values from a normal distribution and averaged over technical duplicates. Data were normalized using z-score and visualized using heat maps. Pathway enrichment analysis was performed using the functional annotations tools on The Database for Annotation, Visualization, and Integrated Discovery (DAVID) (https://davidbioinformatics.nih.gov/).

2.12 | Analysis of Collagen Organization

2.12.1 | Picrosirius Red Staining

Picrosirius red (PSR) staining was used to evaluate the localisation and organization of collagen in tissue sections. The PSR stain solution was prepared by dissolving 0.5 g of Direct Red 80 (Sigma-Aldrich 365 548) in 500 mL saturated aqueous solution of picric acid (Sigma P6744) with a few grains of solid picric acid (Sigma 237 801) added to ensure saturation. Fixed frozen zebrafish cryosections of 10 μm thickness were rapidly defrosted in PBS. They were then washed with PBS (2 × 5 min) to remove any residual OCT compound. Following this, the tissue was stained with PSR stain solution for 1 h. Slides were then submerged in 0.5% acetic acid for 2 × 30 s. Slides were washed in deionized water for 2 × 30 s, followed by dehydration in 95% ethanol for 2 × 20 s and 100% ethanol for 2 × 20 s. Sections were cleared with xylene (Lennox CRTSX0021614) for 2 × 3 min before being covered with 22 × 50 mm No 1.5 glass coverslips (Fisher Scientific 12 383 138) and DPX mounting medium (Sigma 06522-100 ML).

2.12.2 | Polarized Light Microscopy

PSR-stained sections were examined using an upright microscope (Olympus BX43, Tokyo, Japan) equipped with linear

15306860, 2026, 10, Downloaded from https://faseb.onlinelibrary.wiley.com/doi/10.1096/fj.202504935R by University Of California, Los Angeles, Wiley Online Library on [17/06/2026]. See the Terms and Conditions (https://onlinelibrary.wiley.com/terms-and-conditions) on Wiley Online Library for rules of use; OA articles are governed by the applicable Creative Commons License

polarisers (Nikon D-DP polariser and D-DA analyzer) and a color camera (Olympus DP23). To ensure visualization of all collagen fiber orientations and mitigate directional bias inherent to linear polarization, each region of interest was imaged with the polariser and analyzer rotated through 0°, 60°, and 120° relative to the sample [42]. Overview images were acquired using a 0.75 NA 40× Plan APO objective (Olympus, Japan). Images were saved as uncompressed RGB TIFF files (3088 × 2076 pixels). Images for each polariser-analyzer orientation were compiled into a Z-stack using Fiji [43]. A maximum-intensity projection was then applied to generate a single composite image representing the total collagen fiber population within the sampled area.

2.12.3 | Second Harmonic Generation

Second harmonic generation (SHG) microscopy was performed using a custom upright Olympus FV1000MPE-BX61WI multiphoton microscopy system equipped with a pulsed 80 MHz titanium-sapphire laser (Chameleon Ultra, Coherent, USA), and a 1.05 NA water-immersion 25× objective (Olympus). Slides were placed on the stage, and a drop of ultrapure water was added for imaging. SHG was performed with an excitation wavelength of 800 nm. Second harmonic signal collection was achieved using a 420–460 nm bandpass filter. Images were saved as. TIFF files.

2.13 | Statistical Analysis

Unless stated otherwise, statistical analysis was performed using GraphPad Prism, version 8.2.1. Details regarding specific tests are located in the respective figure legends.

3 | Results

3.1 | Zebrafish *rgra* and *rgrb* Paralogs Display Strongest Retinal Expression in the RPE

The canonical role of RGR is to act as a retinal photoisomerase in RPE and Müller cell-mediated visual cycles (Figure 1A). Under photopic conditions, the consensus model is that RGR binds atRAL [4, 19, 23, 24] to photogenerate 11cRAL in the RPE and Müller glia, a process needed to sustain vision. The two zebrafish paralogs of the human *RGR* gene, *rgra* and *rgrb*, encode zebrafish Rgra and Rgrb proteins, respectively [2] (Figure 1B–I). Both display evolutionary protein conservation with human RGR (Figure 1B,C). Zebrafish Rgra and Rgrb are 56.36% or 41.18% conserved with the human RGR protein, respectively, suggesting Rgra might have a higher functional conservation compared to Rgrb (Figure 1B). At the amino acid level, there are important protein features conserved between human, mouse, and zebrafish RGR, including the key retinal chromophore binding lysine ($Lys^{255}/K^{7.43}$) residue, needed for atRAL substrate binding [11]. Additionally, there are seven transmembrane domains and conserved GPCR motifs (Figure 1C).

The spatial and temporal expression of *rgra* and *rgrb* in zebrafish was investigated using existing scRNA-seq datasets [31, 32] (Figure 1D–I). Gene expression in embryonic to larval zebrafish was analyzed using Daniocell (Figure 1D,E). While *rgra* and *rgrb* are predominantly expressed in the eye *rgra* expression was also observed in pigment cells, glial cells/spinal cord, neural cells, mesenchyme and iridophores (Figure S1B). The expression of *rgrb* appears to be more widespread with additional clustering evident in the liver, gut cells, endoderm, exocrine pancreas, xanthophores and pronephros (Figure S1C). This is consistent with a previous study that reported *rgrb* was expressed in the adult liver and gut [7]. Within the larval "eye" subset, the greatest expression for both *rgra* and *rgrb* was *cluster 35*, the RPE, with expression evident throughout the 48–58 to 120 hpf developmental window (Figure 1D,E). Expression was also observed in *Cluster 24*, representing Müller glia cells (Figure 1D,E). This hierarchy of RPE and Müller expression was retained in adult eyes (Figure 1F–I) based on analysis of controls from a light damage scRNA-seq dataset [32]. Overall, the pattern of retinal cell expression is highest for both *rgra* and *rgrb* in the RPE, followed by the Müller glia, but with higher expression of *rgrb* compared to *rgra* in the RPE, and in contrast, higher expression of *rgra* compared to *rgrb* in Müller glia (Figure 1D–I).

3.2 | Generation of *rgra*$^{-/-}$, *rgrb*$^{-/-}$ and *rgrb*$^{-/-}$; *rgra*$^{-/-}$ CRISPR-Cas9 Zebrafish Models

Using CRISPR-Cas9 technology, *rgra*$^{-/-}$ and *rgrb*$^{-/-}$ zebrafish knockout lines were generated. Two CRISPR target sites at exon 2 and exon 4 were selected for *rgra*, which is located on chromosome 13 (Figure 2A). Co-injecting these guides was expected to result in zebrafish embryos with a 2209 bp deletion, which was confirmed in germline *rgra*$^{+/-}$ heterozygous and *rgra*$^{-/-}$ homozygous knockouts by genomic DNA PCR (Figure 2B) and sequencing (*data not shown*). CRISPR guides were chosen to target exon 2 and exon 4 for the *rgrb* gene, which consists of 9 exons, and is located on chromosome 12 (Figure 2A'). Editing at exon 2 did not occur entirely as expected; instead, sequencing results showed a 341 bp deletion created between exons 3 and 4 (*data not shown*). PCR genotyping confirmed the germline *rgrb*$^{+/-}$ heterozygous and *rgrb*$^{-/-}$ homozygous knockout genotypes in subsequent generations (Figure 2B'). At 5 dpf, *rgra*$^{-/-}$ and *rgrb*$^{-/-}$ zebrafish larvae display normal development with no gross morphological abnormalities (Figure 2C). Stable lines of both *rgra* and *rgrb* homozygous knockout lines were bred to adulthood from founder fish and show no gross morphological abnormalities. Given that both paralogs are expressed in the RPE and Müller glia and could display redundancy (Figure 1D–I), double knockout lines were generated from the single knockouts. Individual larvae displaying the correct sized deletion amplicons for *rgra* and *rgrb* confirmed successful generation of double knockout zebrafish (Figure 2B″). At 5 dpf and adulthood, *rgrb*$^{-/-}$; *rgra*$^{-/-}$ double knockout zebrafish display normal development with no gross morphological abnormalities (Figure 2C). To further validate successful generation of the novel single *rgra*$^{-/-}$ or *rgrb*$^{-/-}$ and double *rgrb*$^{-/-}$; *rgra*$^{-/-}$ zebrafish knockout models, mRNA expression was analyzed by qPCR. The significant reduction of *rgra* mRNA only in *rgra*$^{-/-}$ (~60%) and *rgrb*$^{-/-}$; *rgra*$^{-/-}$ (~79%) zebrafish larvae (Figure 2D), as well as the significant reduction of *rgrb* mRNA only in *rgrb*$^{-/-}$ (~77%) and *rgrb*$^{-/-}$; *rgra*$^{-/-}$ zebrafish larvae

15306860, 2026, 10, Downloaded from https://faseb.onlinelibrary.wiley.com/doi/10.1096/fj.202504935R by University Of California, Los Angeles, Wiley Online Library on [17/06/2026]. See the Terms and Conditions (https://onlinelibrary.wiley.com/terms-and-conditions) on Wiley Online Library for rules of use; OA articles are governed by the applicable Creative Commons License

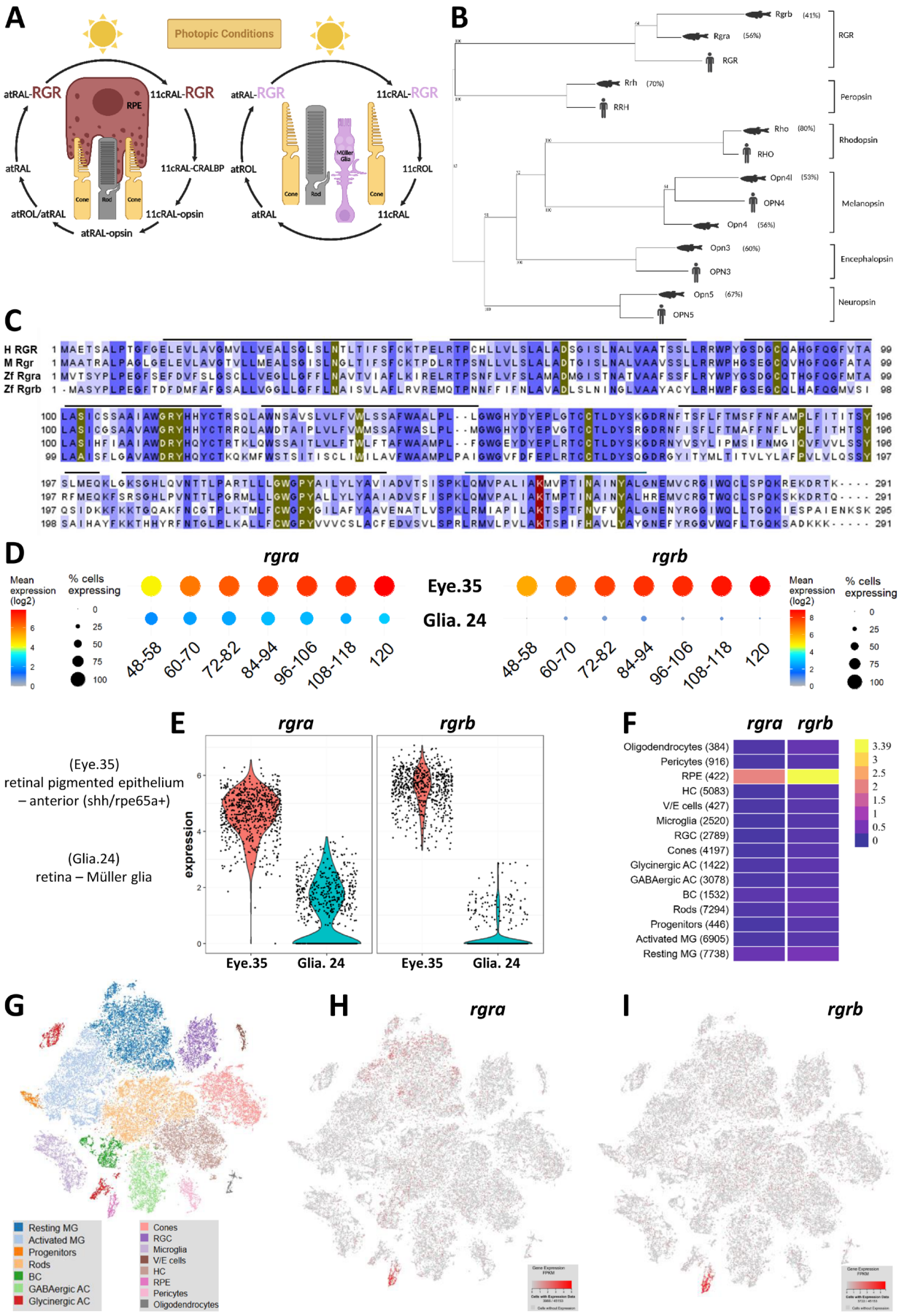

FIGURE 1 | Legend on next page.

15306860, 2026, 10, Downloaded from https://faseb.onlinelibrary.wiley.com/doi/10.1096/fj.202504935R by University Of California, Los Angeles, Wiley Online Library on [17/06/2026]. See the Terms and Conditions (https://onlinelibrary.wiley.com/terms-and-conditions) on Wiley Online Library for rules of use; OA articles are governed by the applicable Creative Commons License

FIGURE 1 | The zebrafish *rgra* and *rgrb* orthologs both display the highest retinal expression in the RPE, with additional expression in the Müller glia. (A) Schematic model of the light-dependent role of RGR in the visual cycle, specifically its roles in the RPE and Müller glia. In these cell types, and under photopic conditions, RGR binds atRAL to generate 11cRAL, which enables vision. Created using biorender website. (B) Phylogenetic tree of representative zebrafish and human non-visual opsin proteins, constructed by a Maximum Likelihood method from an amino acid sequence alignment (see Methods). Branch support values from 100 bootstrap replicates are shown for each internal branch. The percentage represents the level of identical conservation to the human amino acid sequence. (C) Multiple sequence alignment using Clustal Omega multiple sequence alignment tool of the human RGR protein sequence compared to the mouse (M) and zebrafish (Zf) Rgr protein sequences. Annotation using Jalview (https://jalview.org) with blue intensity correlating to percentage identity. The chromophore binding lysine residue linked to substrate binding of RGR to atRAL (red), transmembrane domains (black lines) and conserved G protein coupled receptor (GPCR) motifs (green) are highlighted. (D-E) Expression profile of zebrafish *rgra* and *rgrb* in whole zebrafish larvae generated from the online resource Daniocell https://daniocell.nichd.nih.gov. (D) Profile of *rgra* and *rgrb* expression during zebrafish development, specifically in the RPE (*cluster 35 of the eye*) and the Müller glia (*cluster 24 of the glia*). (E) Violin plot depicting the expression of *rgra* and *rgrb* in zebrafish RPE and Müller glia. (F-I) Profile of *rgra* and *rgrb* expression in the zebrafish retina obtained from the [32] dataset. (F) Heat map displaying the mean expression of *rgra* and *rgrb* in retinal cell types. (G) Expression of *rgra* and *rgrb* in the retina. Here, *rgra* (H), and *rgrb* (I) are predominantly expressed in the RPE, with *rgrb* being more highly expressed in this cell type. There is a stronger expression of *rgra* compared to *rgrb* in the Müller glia.

(~76%) (Figure 2D′) confirmed that the expression of endogenous *rgra*, *rgrb*, or both had been disrupted in their respective bespoke zebrafish lines. Significant downregulation of Rgra and Rgrb proteins was later confirmed via proteomic profiling of eyes from adult $rgrb^{-/-}$; $rgra^{-/-}$ double knockouts (see below).

3.3 | Larval Zebrafish $rgrb^{-/-}$; $rgra^{-/-}$ Double Knockouts Display Impaired Visual Behavior, a Defective Photopic Visual Cycle and Morphological Abnormalities in the RPE-Choroid Interface

Functional vision in *RGR* knockouts has not been investigated in any species. Thus, we used the OKR visual behavior test to determine whether, under standard light rearing conditions, the absence of either *rgra*, *rgrb*, or both paralogs would result in an OKR phenotype. Zebrafish larvae were raised under a normal 14-h light (~450 lx):10-h dark cycle and underwent a standard OKR assay from midday on day five (Figure 3A). Under these conditions, $rgrb^{-/-}$; $rgra^{-/-}$ larvae have a significantly decreased (20.7% reduction) saccadic response compared to WT ($p = 0.0003$), with an average of 16 and 20 saccades per minute (spm), respectively (Figure 3B). This impaired functional vision response was not observed in the single knockouts, as neither $rgra^{-/-}$ (~17 spm, $p = 0.6951$) nor $rgrb^{-/-}$ (~19 spm, $p = 0.7505$) had a significantly different saccadic response compared to WT (18 spm) under the same rearing and assessment conditions (Figure 3C). Therefore, an impaired OKR visual behavior phenotype is only observed in the absence of both *rgra* and *rgrb* under standard conditions, suggesting functional redundancy between the *rgra* and *rgrb* paralogs.

Given the role of RGR in photopic vision, it was hypothesized that the OKR phenotype would be reversed under dark-adapted conditions wherein the canonical RPE65-mediated visual cycle can operate. Thus, zebrafish larvae were raised under a normal 14-h light (~450 lx):10-h dark cycle until ~120 hpf, where they were raised in the dark for an additional ~4.5–6 h before undergoing the standard OKR assay (Figure 3D). Notably, there was no significant difference ($p = 0.4145$) in the saccadic response between WT (17 spm) and $rgrb^{-/-}$; $rgra^{-/-}$ double knockout larvae (16 spm) under dark-adapted conditions (Figure 3E).

To directly determine whether the visual behavior phenotype observed under light-adapted conditions was due to a visual cycle deficiency, the retinoid profile of whole 5 dpf larvae was assessed after they were raised under the same standard light rearing conditions mentioned above (Figure 3F). The absence of both *rgra* and *rgrb* resulted in a significant decrease in 11cRAL levels (54.6%; $p = 0.0357$). There was no significant difference in the levels of total retinoids ($p = 0.9806$), atRAL ($p = 0.5316$), all-*trans*-retinol (atROL) ($p = 0.9629$), all-*trans*-retinal palmitate (atRP) ($p = 0.4798$), 11-*cis*-retinal palmitate (11cRP) ($p = 0.1325$) or 13-*cis*-retinal (13cRAL) ($p = 0.3370$) levels in the absence of both *rgra* and *rgrb* compared to WT (Figure 3G).

Unsurprisingly, this 11cRAL reduction was not observed from larvae which were dark-adapted for 14 h (Figure 3H). Indeed, after dark adaptation, there was no significant difference in the levels of total retinoids ($p = 0.9674$), 11cRAL ($p = 0.4000$), atRAL ($p = 0.4000$), atROL ($p = 0.4115$), atRP ($p = 0.2735$), 9-*cis*-retinal palmitate (9cRP) levels ($p = 0.4000$), 13-*cis*-retinal palmitate (13cRP) ($p = 0.9183$), 11cRP ($p = 0.4000$) or 13cRAL ($p = 0.7552$) levels in *rgra* and *rgrb* double knockouts compared to WT (Figure 3I). Therefore, $rgrb^{-/-}$; $rgra^{-/-}$ larvae display no photopic visual behavior nor visual cycle phenotype when dark-adapted.

Immunostaining of retinal cryosections from <131 hpf zebrafish larvae revealed no change in expression of photoreceptor markers between $rgrb^{-/-}$; $rgra^{-/-}$ larvae and WT controls (Figure 3J,K). In general, retinal morphology in $rgrb^{-/-}$; $rgra^{-/-}$ double knockouts was equivalent to wild-type controls in terms of retinal lamination (Figure 3L,M). However, there was an unexpected gap between the RPE and choroid in the double knockouts (Figure 3M). In summary, $rgrb^{-/-}$; $rgra^{-/-}$ zebrafish larvae, under light-adapted conditions, have significantly decreased photopic vision and impaired photopic visual cycle, with a putative morphological defect in the outer retina–choroid.

15306860, 2026, 10, Downloaded from https://faseb.onlinelibrary.wiley.com/doi/10.1096/fj.202504935R by University Of California, Los Angeles, Wiley Online Library on [17/06/2026]. See the Terms and Conditions (https://onlinelibrary.wiley.com/terms-and-conditions) on Wiley Online Library for rules of use; OA articles are governed by the applicable Creative Commons License

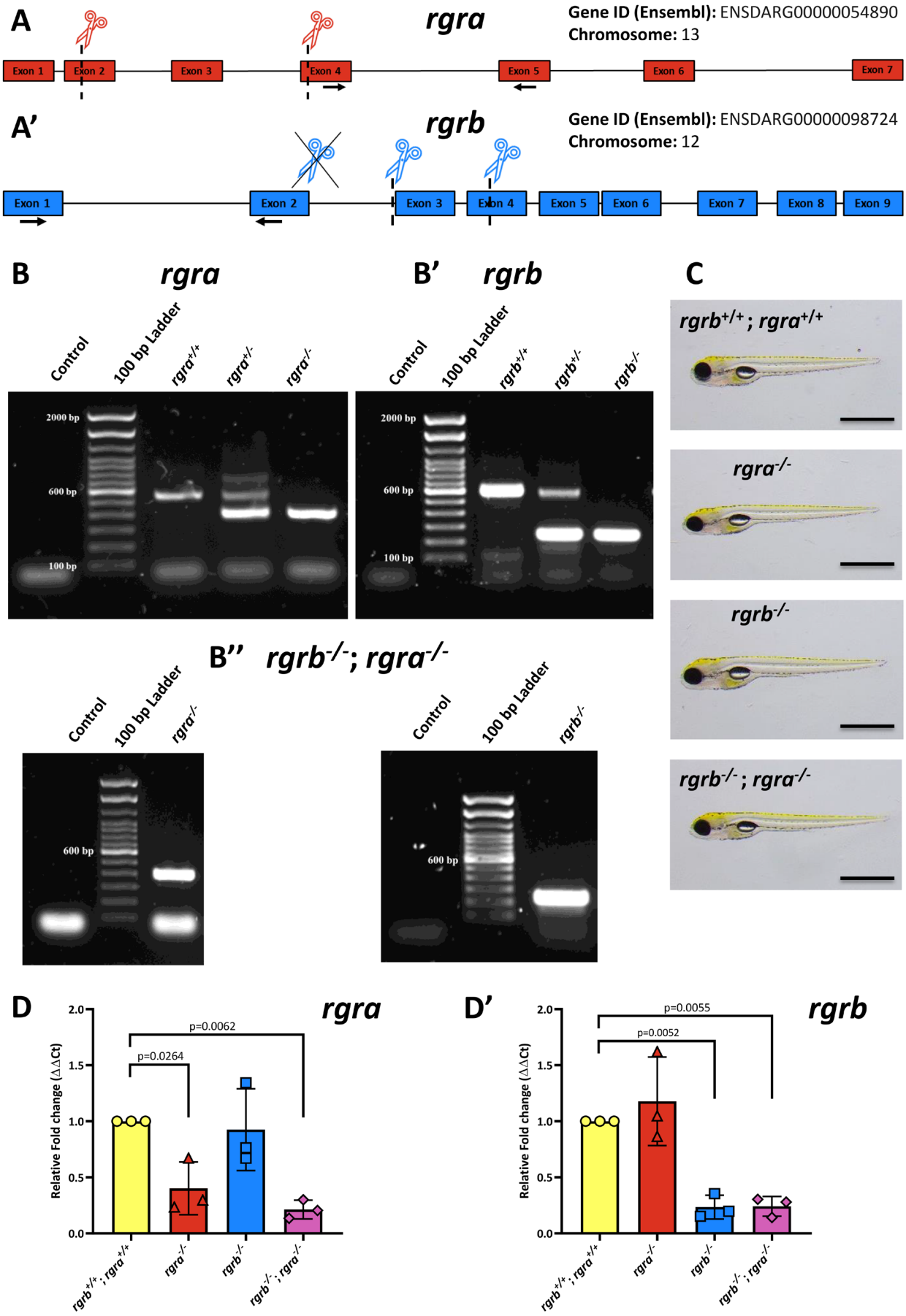

FIGURE 2 | Legend on next page.

15306860, 2026, 10, Downloaded from https://faseb.onlinelibrary.wiley.com/doi/10.1096/fj.202504935R by University Of California, Los Angeles, Wiley Online Library on [17/06/2026]. See the Terms and Conditions (https://onlinelibrary.wiley.com/terms-and-conditions) on Wiley Online Library for rules of use; OA articles are governed by the applicable Creative Commons License

FIGURE 2 | Generation and validation of homozygous single and double *rgrb*$^{-/-}$; *rgra*$^{-/-}$ zebrafish knockout lines. (A) Schematic representation of the CRISPR-Cas9 gene germline editing approach used to generate *rgra* and *rgrb* knockout zebrafish lines. Illustrated by scissors are the target sites at exons 2 and 4, which were anticipated to be cut by the chosen guides, for both *rgra* (A) and *rgrb* (A'). The black hashed lines indicate the site at which a deletion was created. The small arrows represent the location of the qPCR primers. (B) Representative *rgra* PCR genotyping with amplicons of 584 bp and 412 bp representing WT and deletion alleles, respectively. (B′) Representative *rgrb* PCR genotyping with amplicons of 586 bp and 245 bp representing WT and deletion alleles, respectively. (B″) Representative *rgra* and *rgrb* PCR genotyping from an individual *rgrb*$^{-/-}$; *rgra*$^{-/-}$ homozygous double knockout larva. Amplicons of 412 bp and 245 bp represent *rgra* and *rgrb* deletion alleles, respectively. Electrophoresis gels used 1% agarose and a 100 bp DNA ladder. (C) Lateral brightfield microscopy images of *rgrb*$^{+/+}$; *rgra*$^{+/+}$, *rgra*$^{-/-}$, *rgrb*$^{-/-}$ and *rgrb*$^{-/-}$; *rgra*$^{-/-}$ zebrafish larvae at 5 dpf, depicting that there are no obvious morphological defects between them. The scale bar is 100 μm. (D-D′) qPCR graphs representing mean ± standard deviation (SD) of mRNA expression levels for *rgra* (D) and *rgrb* (D′). Data was analyzed by one-way ANOVA, with Dunnett's multiple comparison test, and β-Actin was used as a normalization control. (D) *rgra* mRNA is significantly reduced in *rgra*$^{-/-}$ ($p = 0.0264$) and *rgrb*$^{-/-}$; *rgra*$^{-/-}$ ($p = 0.0062$) zebrafish larvae but not in *rgrb*$^{-/-}$ zebrafish larvae ($p = 0.9543$). $N = 3$, $n = 20$ larvae. (D′) A significant reduction of *rgrb* mRNA is observed in *rgrb*$^{-/-}$ ($p = 0.0052$) and *rgrb*$^{-/-}$; *rgra*$^{-/-}$ zebrafish larvae ($p = 0.0055$) but not for *rgra*$^{-/-}$ zebrafish larvae ($p = 0.6158$). $N = 3$, $n = 20$ larvae.

3.4 | Visual Function Is More Severely Impaired in Larval Zebrafish *rgrb*$^{-/-}$; *rgra*$^{-/-}$ Double Knockout Larvae Under Higher Photopic Light Intensities

As RGR is a photoisomerase [2], we hypothesized that increased environmental light levels would reveal a greater requirement for RGR and worsen the visual behavior and visual cycle phenotypes. Zebrafish larvae were raised under a normal 14-h light (~450 lx):10-h dark cycle until ~120 hpf, then raised under elevated light intensities or durations before undergoing a standard OKR assay (Figure 4A). Zebrafish *rgrb*$^{-/-}$; *rgra*$^{-/-}$ larvae raised under 8 h of 81 Klx have a significantly decreased saccadic response compared to WT (38.4% reduction; $p = 0.0021$), with an average of ~15 and ~9 spm recorded per minute, respectively (Figure 4B). Significantly reduced OKR phenotypes were also apparent when *rgrb*$^{-/-}$; *rgra*$^{-/-}$ larvae were raised for 6 h under either 40-50 Klx (36.7%; $p < 0.0001$) (Figure 4C), or 20–25 Klx (31.7%; $p < 0.0001$) (Figure 4D) compared to WT. The percentage reduction in spm under these three conditions is greater than the percentage reduction observed under standard light rearing conditions. To determine if the enhanced OKR phenotype was reflected by a deficiency in 11cRAL levels, the retinoid profile of whole 5-dpf larvae raised under 40–50 Klx for 6 h was investigated (Figure 4E). A significant decrease in 11cRAL levels (48.8%; $p = 0.0153$) was observed in the absence of both *rgra* and *rgrb* (Figure 4F). Interestingly, this reduction in 11cRAL (48.8% ± 14.65) was not obviously enhanced compared to the 11cRAL reduction observed under standard light conditions (54.6% ± 14.69) (Figure 3G). Furthermore, under the brighter light conditions, there was also no significant difference in total retinoids ($p = 0.1389$), atRAL ($p = 0.1386$), atROL ($p = 0.7597$), atRP ($p = 0.2387$), 11cRP ($p = 0.4000$) or 13cRAL ($p = 0.4178$) levels in the absence of both *rgra* and *rgrb* compared to WT (Figure 4F). In relation to retinal histology, there was no obvious change in expression of protein markers of photoreceptor inner (Zpr1) or outer segments (Prph2) between *rgrb*$^{-/-}$; *rgra*$^{-/-}$ larvae and WT controls when raised under 40–50 Klx for 6 h (Figure 4G,H).

3.5 | There Is no Significant Difference in 11cRAL Levels in Adult *rgrb*$^{-/-}$; *rgra*$^{-/-}$ Zebrafish Raised Under Standard Low Light Housing Conditions

Retinoid levels in post-mortem zebrafish raised under standard low housing light conditions (137 lx) (Figure 5A,B) or after 24 h of dark-adaptation (Figure 5C,D) were investigated. Under low light-adapted conditions, no significant change in the levels of 11cRAL or atRAL was observed in the absence of either *rgra*, *rgrb*, or both paralogs (Figure 5B). Similarly, the absence of *rgra*, *rgrb*, or both paralogs resulted in no significant change in the levels of 11cRAL or atRAL under dark-adapted conditions (Figure 5D).

In relation to changes in other retinoids (Figure 5B,D), there was a significant increase in atROL levels observed between *rgrb*$^{-/-}$; *rgra*$^{-/-}$ versus WT adult zebrafish eyes ($p = 0.0132$) under standard lighting, whereas in dark-adapted conditions, there was only a significant ($p = 0.0021$) increase in atROL levels observed between *rgrb*$^{-/-}$; *rgra*$^{-/-}$ double knockouts versus *rgrb*$^{-/-}$ single knockouts. In contrast, in dark-adapted conditions, there is a significant increase in atRP levels in the double knockouts compared to *rgra*$^{-/-}$ ($p = 0.0175$) and *rgrb*$^{-/-}$ ($p = 0.0431$), with only significant differences in atRP levels observed between the double knockouts and *rgra*$^{-/-}$ ($p = 0.0459$) in light-adapted conditions. No significant changes were detected between WT, *rgra*$^{-/-}$, *rgrb*$^{-/-}$ or *rgrb*$^{-/-}$; *rgra*$^{-/-}$ for 11-*cis*-retinol (11cROL), 11cRP or 9cRP levels in light-adapted adult zebrafish. Indeed, the only other significant differences between the double knockouts and WT were reduced 9cRAL ($p = 0.0074$) and increased 9cRP ($p = 0.0005$), and increased 13cRP ($p = 0.0283$) after dark adaptation.

In summary, under dark-adapted and low light-adapted conditions, in the absence of endogenous *rgra*, *rgrb*, or both paralogs, there was no significant change in 11cRAL levels for *rgrb*$^{-/-}$; *rgra*$^{-/-}$ adult zebrafish.

3.6 | Proteome Profiling of Adult *rgrb*$^{-/-}$; *rgra*$^{-/-}$ Zebrafish Eyes Reveals Significant Upregulation of ECM Proteins, With Disrupted Collagen Fibril Organization in Bruch's Membrane

Given that adult *rgrb*$^{-/d}$; *rgra*$^{-/-}$ zebrafish did not have a visual cycle deficit in low light and ethical constraints for in vivo analyses, we decided to conduct unbiased proteomic profiling of whole adult zebrafish eyes to determine which proteins and pathways are dysregulated in the absence of both Rgra and Rgrb. 179 proteins were differentially expressed from the 9107 proteins detected, wherein proteins were filtered for a significant p value of < 0.05 and a fold change of > 2 (Figure 6A). The heat map demonstrates how the individual biological replicates for respective genotypes cluster

15306860, 2026, 10, Downloaded from https://faseb.onlinelibrary.wiley.com/doi/10.1096/fj.202504935R by University Of California, Los Angeles, Wiley Online Library on [17/06/2026]. See the Terms and Conditions (https://onlinelibrary.wiley.com/terms-and-conditions) on Wiley Online Library for rules of use; OA articles are governed by the applicable Creative Commons License

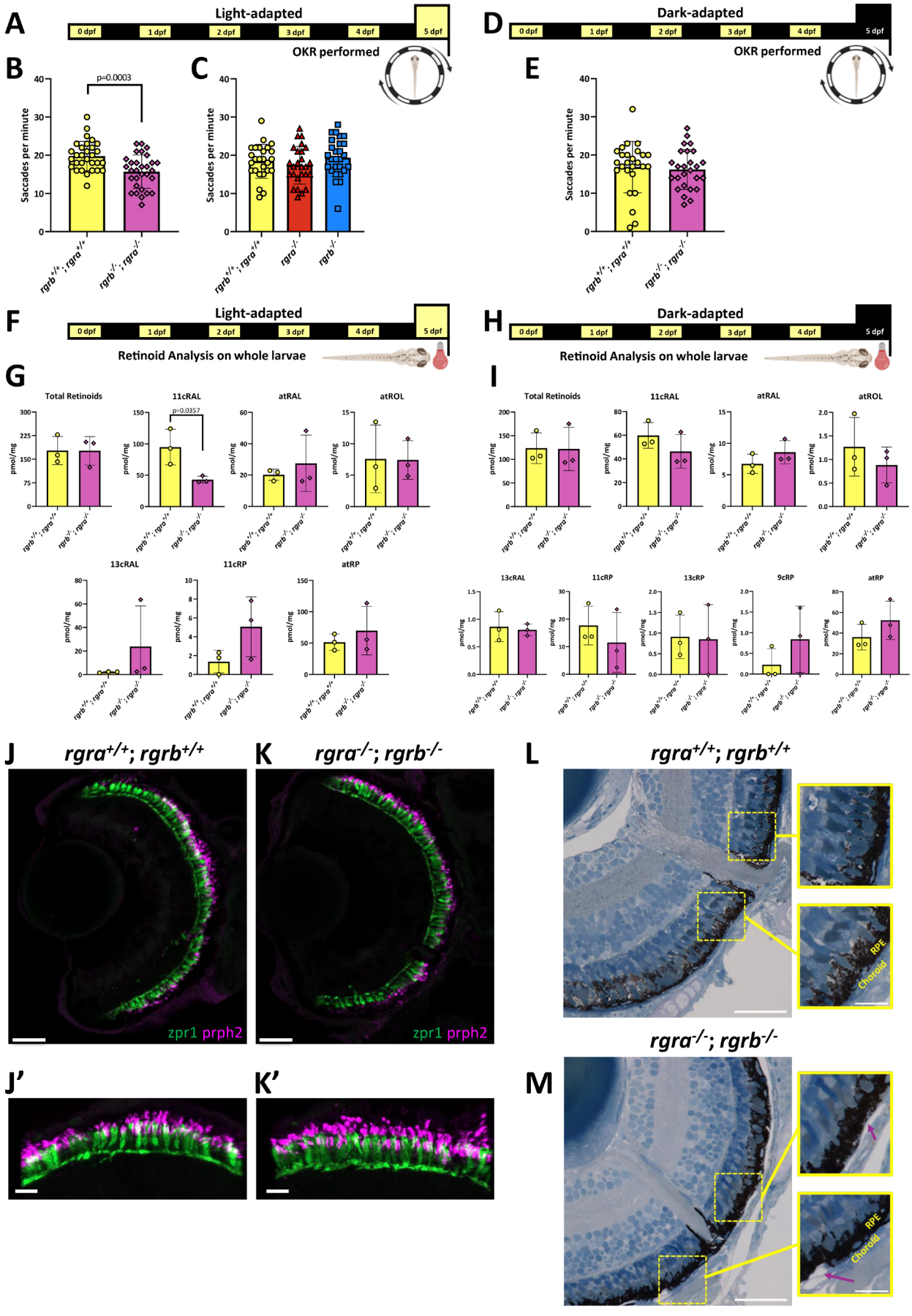

FIGURE 3 | Legend on next page.

15306860, 2026, 10, Downloaded from https://faseb.onlinelibrary.wiley.com/doi/10.1096/fj.202504935R by University Of California, Los Angeles, Wiley Online Library on [17/06/2026]. See the Terms and Conditions (https://onlinelibrary.wiley.com/terms-and-conditions) on Wiley Online Library for rules of use; OA articles are governed by the applicable Creative Commons License

FIGURE 3 | Zebrafish *rgrb*$^{-/-}$; *rgra*$^{-/-}$ double knockout larvae show significantly impaired visual behavior and reduced 11cRAL levels. (A,D,F,H) Schematics illustrating the different environmental light rearing paradigms and downstream functional or biochemical assays. (B-C) Zebrafish larvae were raised under a 14-h light (~450 lx):10-h dark cycle until 124 hpf (~midday on day 5) before undergoing a standard OKR assay until ~126 hpf. (B) There is a significant reduction in saccadic response between WT and *rgrb*$^{-/-}$; *rgra*$^{-/-}$ double knockout larvae ($p = 0.0003$) under standard rearing conditions. $N = 3$, $n = 10$. (C) In contrast, there is no significant difference in saccadic response between WT and *rgra*$^{-/-}$ ($p = 0.6951$), or *rgrb*$^{-/-}$ ($p = 0.7505$) single knockout larvae. $N = 4$, $n = 6$–7. (D) Schematic illustrating rearing paradigm where zebrafish larvae were raised under a 14-h light (~450 lx):10-h dark cycle until ~120 hpf, then raised under dark conditions until ~124.5 hpf, before undergoing a standard OKR assay until 126 hpf. (E) Notably, in the dark-adapted *rgrb*$^{-/-}$; *rgra*$^{-/-}$ larvae, there is no significant difference in saccadic response between WT and *rgrb*$^{-/-}$; *rgra*$^{-/-}$ larvae ($p = 0.4145$). $N = 3$, $n = 8/9$. The OKR graphs (B, C, E) represent the mean ± SD, with each dot representing an individual zebrafish larva. (F) Zebrafish were raised as per (A) but collected under dim red light for retinoid analysis. (G) The retinoid profiles of 5 dpf *rgrb*$^{-/-}$; *rgra*$^{-/-}$ whole larvae and WT controls raised under standard light conditions. 11cRAL levels are significantly decreased in *rgrb*$^{-/-}$; *rgra*$^{-/-}$ larvae ($p = 0.0357$). Total retinoids ($p = 0.9806$), atRAL ($p = 0.5316$), atROL ($p = 0.9629$), atRP ($p = 0.4798$), 11cRP levels ($p = 0.1325$) and 13cRAL ($p = 0.3370$) levels are not significantly altered in the absence of both *rgra* and *rgrb*. (H) Schematic of experimental conditions where zebrafish larvae were raised under a 14-h light (~450 lx):10-h dark cycle until ~120 hpf. At this point, larvae were raised under dark conditions until 124 hpf (~midday on day 5). (I) The retinoid profiles of 5 dpf *rgrb*$^{-/-}$; *rgra*$^{-/-}$ whole larvae and WT controls raised under dark-adapted conditions. Total retinoids ($p = 0.9674$), 11cRAL ($p = 0.4000$), atRAL ($p = 0.4000$), atROL levels ($p = 0.4115$), atRP ($p = 0.2735$), 9cRP levels ($p = 0.4000$), 13cRP ($p = 0.9183$), 11cRP ($p = 0.4000$), and 13cRAL ($p = 0.7552$) levels are not significantly different in the absence of both *rgra* and *rgrb*. For retinoid analysis, 51 whole larvae were collected under dim red light, with retinoids being profiled by HPLC. The graphs (G,I) represent the mean ± SD, and three biological replicates ($N = 3$, $n = 51$). (J-K) Images of retinal cross sections from 5 dpf WT controls (J) and *rgrb*$^{-/-}$; *rgra*$^{-/-}$ (K) zebrafish larvae stained with antibodies to zpr1 (cone photoreceptors, green) and prph2 (outer segment, magenta). Sections were imaged with a 20× objective (J-K) and 63× objective (J'-K'). Scale bar = 30 μm (J-K) and 10 μm (J'-K'). (L-M) Representative brightfield images of 5 dpf WT controls (L) and *rgrb*$^{-/-}$; *rgra*$^{-/-}$ (M) zebrafish larvae retinal cross sections stained with toluidine blue. Images obtained with a 100× objective. $N = 2$, $n = 2$. Scale bars: Overview 30 μm, inset: 10 μm. Data were analyzed by an unpaired two-tailed *t*-test, if it passed the Shapiro–Wilk test or a Mann–Whitney test if the dataset did not. Dataset C was evaluated for normality and homoscedasticity using residual-based diagnostic tests. Having met the assumptions of normality and equal variances, group differences were assessed using a one-way ANOVA (F-test) and post hoc analysis using Tukey's multiple comparison test as it passed the Shapiro–Wilk test.

closely together (Figure 6B). From the aforementioned cutoffs, 139 proteins were identified as significantly upregulated, with 40 proteins significantly downregulated in *rgrb*$^{-/-}$; *rgra*$^{-/-}$ zebrafish compared to WT (full list in supplemental documentation). Rgra and Rgrb were two of the most highly downregulated proteins displaying ~72 and ~30 fold reduction compared to WT, providing additional evidence that *rgrb*$^{-/-}$; *rgra*$^{-/-}$ zebrafish were generated successfully (Figure 6C). The significantly differentially expressed proteins were processed for pathway enrichment analysis. The corresponding top KEGG pathways were "*cytoskeleton in muscle cells*", *"focal adhesion"* and *"ECM-receptor interaction"* (Figure 6D). Gene ontology (GO) uncovered differentially expressed proteins for the biological process terms *"cell adhesion"*, *"cell–cell adhesion"* and "*extracellular matrix organisation*" (Figure 6E) and for the molecular function terms "*calcium ion binding*", "*structural molecular activity*" and "*actin filament binding*" (Figure 6F). This was surprising based on the proposed role of RGR in the visual cycle. Indeed, there were minimal differentially expressed "*visual cycle"* proteins (Figure 6G). *lratb.1* (~1.4 fold change) was significantly upregulated, and *rpe65a* (~−1.3 fold change) was significantly downregulated in the *rgrb*$^{-/-}$; *rgra*$^{-/-}$ zebrafish. In our previous study, loss of the visual cycle protein Rlbp1b led to upregulation of Rgra and Rgrb proteins [34]. Here, however, this relationship was not reciprocal, as neither Cralbpa nor Cralbpb were significantly altered ($p = 0.372$ and 0.744, respectively) in the *rgrb*$^{-/-}$; *rgra*$^{-/-}$ double knockouts. Intriguingly, proteins related to ECM structure and organization were significantly differentially expressed in the *rgrb*$^{-/-}$; *rgra*$^{-/-}$ zebrafish double knockouts (Figure 6H). Collagen alpha-1 (XI) chain isoform X1 (3.03 fold change), collagen alpha-1 (XI) chain (6.67 fold change) and collagen alpha-1 (XII) chain isoform X1 (4.99 fold change) are examples of ECM proteins related to structure and organization, which are significantly upregulated in the *rgrb*$^{-/-}$; *rgra*$^{-/-}$ zebrafish. This was surprising given that there have been no studies linking the absence of Rgr to disrupted ECM.

To further investigate the upregulated ECM, we used PSR staining and polarized light microscopy to detect fibrillar collagen. Notably, collagen fibril organization in Bruch's membrane was disrupted in the absence of *rgra* and *rgrb* (Figure 6I,J). The Bruch's membrane from WT controls has a regular, ladder-like architecture with lateral collagen fibrils bordering a central, fibril-free space (black), connected by perpendicular bridging fibrils at 3–10 μm intervals (Figure 6I). In contrast, the Bruch's membrane from *rgrb*$^{-/-}$; *rgra*$^{-/-}$ double knockouts displayed a greater abundance of disorganized collagen fibrils, which filled the characteristic collagen-free area between the inner and outer collagen fiber bands that are evident in the WT (Figure 6J). The collagen fiber count was significantly increased for *rgrb*$^{-/-}$; *rgra*$^{-/-}$ zebrafish compared to WT ($p = 0.0355$), but the collagen fiber width was not ($p = 0.066$) (Figure S2). Disruption of the collagen fiber organization of Bruch's membrane was also observed in *rgrb*$^{-/-}$; *rgra*$^{-/-}$ zebrafish by SHG microscopy (Figure S3).

4 | Discussion

The aim of this study was to enhance understanding of the biological role of RGR in vivo, using a model organism with a retina enriched in cone photoreceptors. Thus, novel *rgra*$^{-/-}$, *rgrb*$^{-/-}$, and *rgrb*$^{-/-}$; *rgra*$^{-/-}$ double knockout zebrafish models were generated. Zebrafish *rgrb*$^{-/-}$; *rgra*$^{-/-}$ larvae display reduced optokinetic visual behavior, a phenotype which was enhanced under brighter photopic conditions. Adult double knockouts displayed

15306860, 2026, 10, Downloaded from https://faseb.onlinelibrary.wiley.com/doi/10.1096/fj.202504935R by University Of California, Los Angeles, Wiley Online Library on [17/06/2026]. See the Terms and Conditions (https://onlinelibrary.wiley.com/terms-and-conditions) on Wiley Online Library for rules of use; OA articles are governed by the applicable Creative Commons License

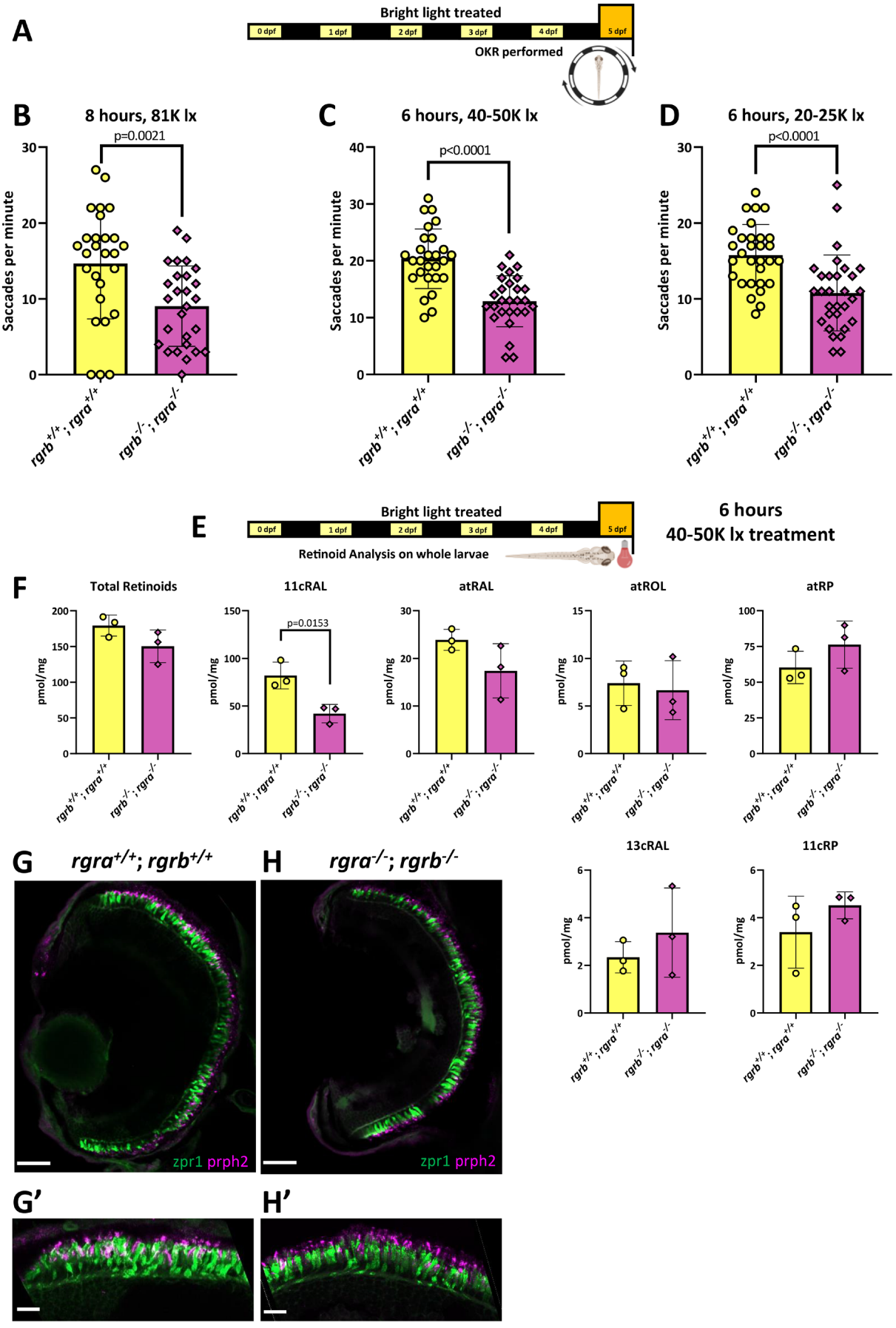

FIGURE 4 | Legend on next page.

15306860, 2026, 10, Downloaded from https://faseb.onlinelibrary.wiley.com/doi/10.1096/fj.202504935R by University Of California, Los Angeles, Wiley Online Library on [17/06/2026]. See the Terms and Conditions (https://onlinelibrary.wiley.com/terms-and-conditions) on Wiley Online Library for rules of use; OA articles are governed by the applicable Creative Commons License

FIGURE 4 | The OKR visual behavior deficit in *rgrb*$^{-/-}$; *rgra*$^{-/-}$ larvae is heightened under higher light intensities. (A) A schematic diagram illustrating how zebrafish larvae were raised under a 14-h light (~450 lx):10-h dark cycle until ~120 hpf. At this point, larvae were raised under either 81 K lx for 8 h (B) or 6 h of either 40-50 K lx (C) or 20–25 K lx (D). After the treatment, they underwent a standard OKR assay. (B) There is a significant difference in saccadic response between WT and *rgrb*$^{-/-}$; *rgra*$^{-/-}$ larvae ($p = 0.0021$) following an 8-h bright light treatment of 81 K lx. $N = 3$, $n = 7$–10. (C) There is a significant difference in saccadic response between WT and *rgrb*$^{-/-}$; *rgra*$^{-/-}$ larvae ($p < 0.0001$) following a 6-h bright light treatment of 40–50 K lx. $N = 3$, $n = 8$–11. (D) There is a significant difference in saccadic response between WT and *rgrb*$^{-/-}$; *rgra*$^{-/-}$ larvae ($p < 0.0001$) following a 6-h bright light treatment of 20–25 K lx. $N = 3$, $n = 10$. The OKR graphs (B-D) represent the mean ± SD, with each dot representing an individual zebrafish larva. (E) Schematic diagram illustrating how zebrafish larvae were raised under a 14-h light (~450 lx):10-h dark cycle until ~120 hpf. At this point, larvae were kept under 40–50 K lx for 6 h prior to retinoid analysis (F) or immunostaining (G-H). (F) The retinoid profiles of 5 dpf *rgrb*$^{-/-}$; *rgra*$^{-/-}$ whole larvae and WT controls raised under 40–50 K lx for 6 h. 11cRAL levels are significantly decreased in *rgrb*$^{-/-}$; *rgra*$^{-/-}$ larvae ($p = 0.0153$). Total retinoids ($p = 0.1389$), atRAL ($p = 0.1386$), atROL ($p = 0.7597$), atRP ($p = 0.2387$), 11cRP ($p = 0.4000$) and 13cRAL ($p = 0.4178$) levels are not significantly altered in the absence of *rgra* and *rgrb*. For retinoid analysis, 51 whole larvae were collected under dim red light (E), with retinoids being profiled by HPLC. The graphs represent the mean ± SD, and three biological replicates ($N = 3$, $n = 51$). Data was analyzed by an unpaired two-tailed *t*-test if it passed the Shapiro–Wilk test or a Mann–Whitney test if the dataset did not. (G-H) Images of retinal cross sections from WT (G) and *rgrb*$^{-/-}$; *rgra*$^{-/-}$ (H) zebrafish larvae stained with antibodies to zpr1 (cone photoreceptors, green) and prph2 (outer segment, magenta). Sections were imaged with a 20× objective (G-H) and 63× objective (G′-H′). Scale bar = 30 μm (G-H) and 10 μm (G′-H′).

increased ECM proteins and increased collagen fibers in Bruch's membrane at the RPE-choroid interface.

There are no prior publications using the cone-dominant zebrafish to study RGR. Like many genes, genome duplication resulted in the presence of two *RGR* paralogs in the zebrafish genome. Similar to the human *RGR* gene, *rgra* consists of 7 exons, while *rgrb* consists of 9 exons. The 41%–56% protein conservation of the zebrafish Rgra and Rgrb proteins with human RGR, in addition to the conservation of the retinal chromophore binding residue, supports the translational relevance of zebrafish for RGR biology.

Using two scRNA-seq databases, we elucidated that from early development through to adulthood, both *rgra* and *rgrb* are expressed in the RPE, with *rgrb* displaying moderately higher RPE expression. Lower levels of both paralogs are expressed in the Müller glia, albeit *rgra* expression is moderately stronger in this cell type compared to *rgrb*. RGR transcript expression has previously been reported in the RPE and Müller glia; however, there are species differences in which cell type has higher expression [9–12]. In the zebrafish retina, while the RPE is the major site of expression for both *rgra* and *rgrb*, lower levels of expression are observed in the Müller glia, being more similar to RGR in the human retina than the pattern in bovine or mouse retina [11].

Surprisingly, both *rgra* and *rgrb* retain expression in RPE and Müller glia. The whole-genome duplication that occurred in teleosts often leads to subfunctionalised expression of duplicated paralogs in different cell types. The conserved high expression of *rgra* and *rgrb* in the RPE and Müller glia suggests a unique, robust evolutionary requirement for *rgra* and *rgrb* to be expressed in the same cell types, which could result in functional redundancy. Indeed, it was only in the absence of both *rgra* and *rgrb* that the prevalent phenotypes of this study were revealed.

The *rgra* and *rgrb* double knockouts are viable and produce offspring. We undertook visual behavior analyses, retinoid profiling and histological analysis to investigate the consequence of loss of both Rgra and Rgrb on photopic vision, the photopic visual cycle and the morphological integrity of the retina. Our original findings demonstrate that loss of *rgra* and *rgrb* results in decreased OKR saccadic frequency, plus reduced 11cRAL levels following rearing under standard light conditions. A significant reduction in OKR is not apparent following dark adaptation. The lack of visual behavior, or related visual cycle phenotypes after dark adaptation, corroborates the predominant role of RGR in photopic conditions. Indeed, previous findings in rod-dominant *Rgr*$^{-/-}$ mice dark-adapted for 12 h reported no significant change in total retinal or 11cRAL levels compared to WT, suggesting alternative visual cycle pathways can compensate for the loss of RGR during dark adaptation [20]. The generation of the visual chromophore via the "classical visual cycle" is known to rely on RPE65, which can generate 11cRAL for vision in light and dark conditions, but under photopic conditions cannot generate sufficient 11cRAL for vision.

After identifying a robust OKR phenotype (20.7% reduction) in the *rgrb*$^{-/-}$; *rgra*$^{-/-}$ zebrafish larvae under standard light rearing conditions (~450 lx), larvae were exposed to either 8 h of 81 K lx or 6 h of either 40-50 K or 20-25 K lx. Notably, increasing light levels resulted in stronger functional vision phenotypes, providing direct evidence that the requirement of RGR for photopic vision is light-level dependent. This is in agreement with a previous study of retinal electrophysiology in rod-dominant *Rgr*$^{-/-}$ mice [20].

It was initially surprising that adult *rgrb*$^{-/-}$; *rgra*$^{-/-}$ zebrafish had no significant decrease in 11cRAL levels. However, the level of environmental light in which they were raised is ~3 times lower than the standard light conditions in which the *rgrb*$^{-/-}$; *rgra*$^{-/-}$ zebrafish larvae were raised. This is consistent with *Rgr*$^{-/-}$ knockout mice raised under 140 lx that display no significant difference in 11cRAL levels compared to WT [20]. The generation of 13-*cis* and 9-*cis* retinoids is associated with thermal isomerisation and not just enzymatic or photopic generation. In the absence of *rgra*, 13cRAL and 9cRAL levels were increased under both light and dark conditions. While speculative, it could be interpreted that *rgra* is involved in clearing 13cRAL and 9cRAL. In the dark, the absence of both *rgra* and *rgrb* resulted in reduced 9cRAL levels and a concomitant increase in 9cRP levels.

15306860, 2026, 10, Downloaded from https://faseb.onlinelibrary.wiley.com/doi/10.1096/fj.202504935R by University Of California, Los Angeles, Wiley Online Library on [17/06/2026]. See the Terms and Conditions (https://onlinelibrary.wiley.com/terms-and-conditions) on Wiley Online Library for rules of use; OA articles are governed by the applicable Creative Commons License

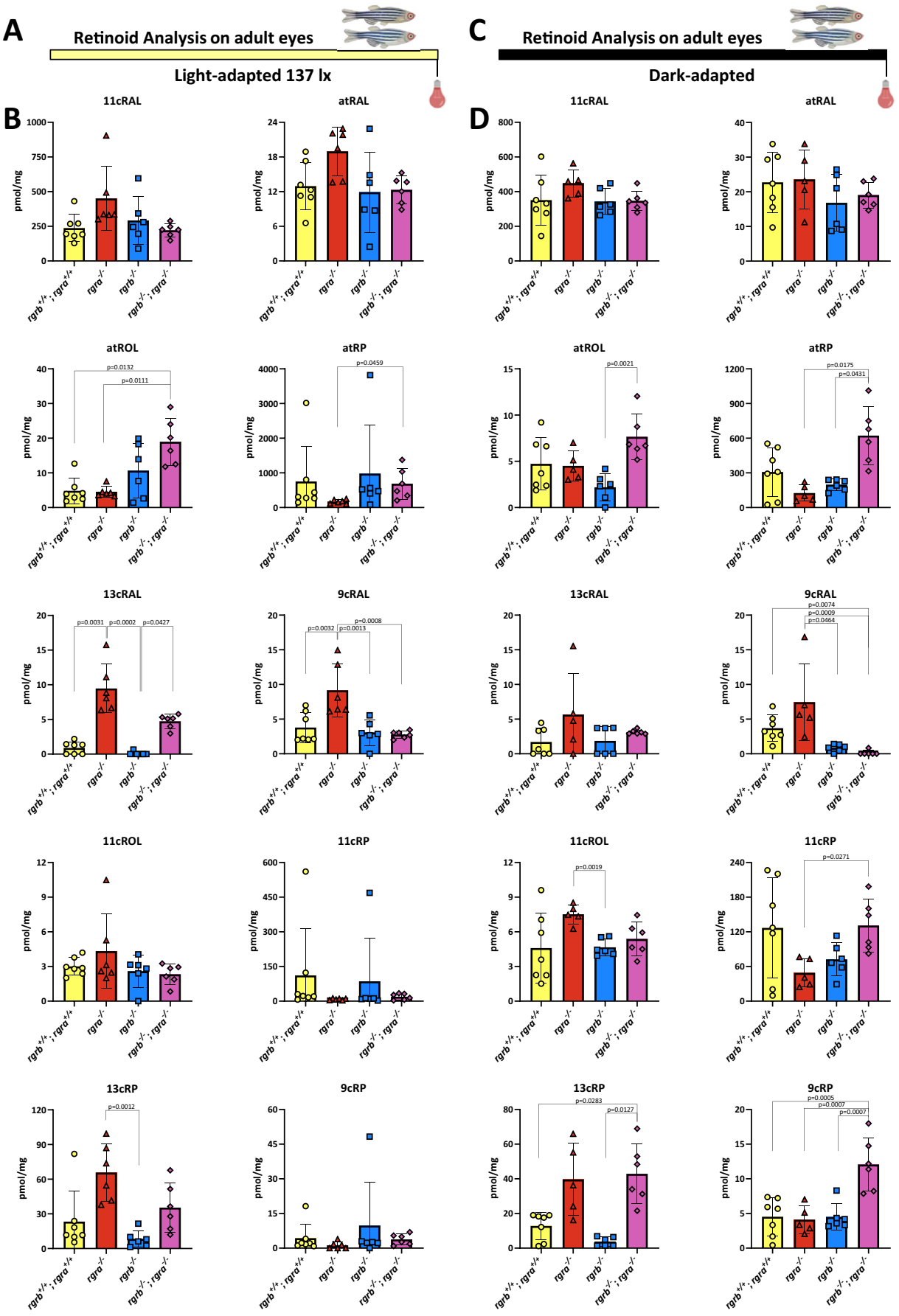

FIGURE 5 | Legend on next page.

15306860, 2026, 10, Downloaded from https://faseb.onlinelibrary.wiley.com/doi/10.1096/fj.202504935R by University Of California, Los Angeles, Wiley Online Library on [17/06/2026]. See the Terms and Conditions (https://onlinelibrary.wiley.com/terms-and-conditions) on Wiley Online Library for rules of use; OA articles are governed by the applicable Creative Commons License

FIGURE 5 | 11cRAL levels are not significantly decreased in the absence of *rgra*, *rgrb*, or both paralogs for adult zebrafish under standard low light conditions or dark-adapted conditions. (A) Schematic diagram representing the experimental conditions where adult zebrafish were raised under light-adapted conditions (137 lx) prior to the collection of their eyes under dim red light. (B) The retinoid profiles of eyes from adult zebrafish raised under standard low light conditions. 11cRAL, atRAL, 11cROL, 11cRP and 9cRP levels were not significantly reduced in the absence of *rgra*, *rgrb*, or both paralogs under light-adapted conditions. There was a significant change in the levels of atROL between $rgrb^{+/+}$; $rgra^{+/+}$ and $rgrb^{-/-}$; $rgra^{-/-}$ adult zebrafish ($p = 0.0132$) and in the atRP levels between $rgra^{-/-}$ and $rgrb^{-/-}$; $rgra^{-/-}$ ($p = 0.0459$). A significant difference in 13cRAL levels was observed between $rgrb^{+/+}$; $rgra^{+/+}$ and $rgra^{-/-}$ ($p = 0.0031$), $rgra^{-/-}$ and $rgrb^{-/-}$ ($p = 0.0002$) and $rgrb^{-/-}$ and $rgrb^{-/-}$; $rgra^{-/-}$ ($p = 0.0427$). There was a significant difference in 9cRAL levels between $rgrb^{+/+}$; $rgra^{+/+}$ and $rgra^{-/-}$ ($p = 0.0032$), $rgra^{-/-}$ and $rgrb^{-/-}$ ($p = 0.0013$) and $rgra^{-/-}$ and $rgrb^{-/-}$; $rgra^{-/-}$ ($p = 0.0008$). There was a significant difference in 13cRP levels between $rgra^{-/-}$ and $rgrb^{-/-}$ ($p = 0.0012$). (C) Schematic diagram of experimental conditions where adult zebrafish were dark-adapted for 24 h prior to the collection of their eyes under dim red light. (D) The retinoid profiles of eyes from adult zebrafish raised under dark-adapted conditions. 11cRAL, atRAL and 13cRAL levels are not significantly reduced in the absence of *rgra*, *rgrb* or both paralogs. There was a significant difference in the levels of atROL between $rgrb^{-/-}$ and $rgrb^{-/-}$; $rgra^{-/-}$ adult zebrafish ($p = 0.0021$) and in the atRP levels between $rgra^{-/-}$ and $rgrb^{-/-}$; $rgra^{-/-}$ ($p = 0.0175$), and $rgrb^{-/-}$ and $rgrb^{-/-}$; $rgra^{-/-}$ ($p = 0.0431$). A significant difference in 9cRAL levels between $rgrb^{+/+}$; $rgra^{+/+}$ and $rgrb^{-/-}$; $rgra^{-/-}$ ($p = 0.0074$), $rgra^{-/-}$ and $rgrb^{-/-}$ ($p = 0.0464$) and $rgra^{-/-}$ and $rgrb^{-/-}$; $rgra^{-/-}$ ($p = 0.0009$) was observed, in addition to a significant difference in 13cRP levels between $rgrb^{+/+}$; $rgra^{+/+}$ and $rgrb^{-/-}$; $rgra^{-/-}$ ($p = 0.0283$) and $rgrb^{-/-}$ and $rgrb^{-/-}$; $rgra^{-/-}$ ($p = 0.0127$). There was also a significant difference in 9cRP levels between $rgrb^{+/+}$; $rgra^{+/+}$ and $rgrb^{-/-}$; $rgra^{-/-}$ ($p = 0.0005$), $rgra^{-/-}$ and $rgrb^{-/-}$; $rgra^{-/-}$ ($p = 0.0007$) and $rgrb^{-/-}$ and $rgrb^{-/-}$; $rgra^{-/-}$ ($p = 0.0007$). Retinoids were profiled by HPLC. Graphs represent the mean ± SD, with each symbol representing a biological replicate. Prior to statistical testing, data were evaluated for normality and homoscedasticity using residual-based diagnostic tests. For datasets meeting the assumptions of normality and equal variances, group differences were assessed using a one-way ANOVA (F-test) and post hoc analysis using Tukey's multiple comparison test if it passed the Shapiro–Wilk test. When datasets met the assumptions of normality but not equal variances, group differences were assessed using Welch's one-way ANOVA, with the Dunnett T3 test used as the post hoc analysis test. When normality assumptions were not met, a Kruskal–Wallis test was applied. Post hoc analysis was Dunn's multiple comparisons test.

We chose unbiased proteomic profiling as an alternative, ex vivo means to evaluate the effects of loss of Rgra and Rrgb on the zebrafish eye. Interestingly, there was little disruption to proteins related to the "visual cycle" such as Cralbpa, Cralbpb, and Rdh5. The zebrafish orthologues of *lratb.1* and *rpe65a* are upregulated and downregulated, respectively, in the absence of *rgra* and *rgrb*. LRAT converts atROL to generate atREs, which are substrates for RPE65 to generate 11cROL. LRAT and RPE65 are important proteins needed for the canonical visual cycle [44], which may be partially compensating for the lack of *rgra* and *rgrb*. Notably, LRAT's substrate atROL is significantly increased in the light-adapted adult $rgrb^{-/-}$; $rgra^{-/-}$ zebrafish compared to WT. However, this theory is not consistent with the observed downregulation of Rpe65a.

Interestingly, the proteomic data uncovered an upregulation of proteins associated with ECM structure and organization. These include several collagen alpha proteins. For example, there is an upregulation in the zebrafish orthologues of Col11a1a and Col11a1b. To validate the novel finding that ECM proteins are upregulated in adult $rgrb^{-/-}$; $rgra^{-/-}$ zebrafish, adult retinal sections were stained with PSR, a histological stain to visualize collagen fibers. Bruch's membrane is relevant in this context as it is a collagen-rich area between the RPE and choroid, composed of an inner and outer collagenous layer in addition to an elastin layer. Bruch's membrane is clinically relevant as some patients with a dominant RGR variant exhibit loss of outer retinal layers [14] and deposits of a RGR splice variant are found in Bruch's membrane [17, 18]. Importantly, the absence of both *rgra* and *rgrb* caused a disruption to the collagen fibril organization within Bruch's membrane, with disorganized collagen fiber bundles filling the entire space in comparison to the two clear collagen fiber bundles separated by a collagen-free space in WT controls. To our knowledge, there are no prior studies which directly report a Bruch's membrane phenotype in *Rgr* knockout models [12, 20]. Previous reports state the retina of $Rgr^{-/-}$ knockout mice raised under 9 months of cyclic house lighting appeared histologically normal, and retinal degeneration was not evident [20]. Likewise, a transgenic *Rgr* mouse with no retinal degeneration was not assessed for Bruch's membrane disruption [12].

We can only speculate on how loss of RGR could lead to excess collagen in Bruch's membrane. Conceivably, cellular stress in the RPE and Müller glia arising from a defective visual cycle could result in inflammation, activation of TGF-β, epithelial to mesenchymal transition and overproduction of collagen. Müller glia can sense mechanical changes in the whole retinal thickness and produce ECM constituents, and during retinal diseases, secrete profibrotic and proinflammatory factors and ECM components as they transition to a myofibroblast state [45]. Müller glia also secrete Collagen IV, which has been detected in Bruch's membrane [45]. Collagen deposition has been reported for other inherited retinal genes. Wide-spaced collagen was detected in Bruch's membrane of *Efemp1*-R345W knockin mice [46]. This point mutation in the *EFEMP1* gene is linked to Doyne honeycomb retinal dystrophy/Malattia Leventinese with deposits between Bruch's membrane and the RPE [46].

In summary, this study is the first to demonstrate evidence of a visual behavior phenotype in an *Rgr* knockout model. The functional vision phenotype is light dependent, as would be expected for a photoisomerase and is also concomitant with significant reductions in the visual cycle chromophore 11cRAL. Intriguingly, unbiased proteomic profiling revealed little change in the expression of other visual cycle proteins. Instead, and unexpectedly, loss of RGR in the adult retina was associated with significant increases in ECM proteins. Histological analysis determined that this resulted in significantly higher levels of collagen in Bruch's membrane, an ECM-rich structure between the

15306860, 2026, 10, Downloaded from https://faseb.onlinelibrary.wiley.com/doi/10.1096/fj.202504935R by University Of California, Los Angeles, Wiley Online Library on [17/06/2026]. See the Terms and Conditions (https://onlinelibrary.wiley.com/terms-and-conditions) on Wiley Online Library for rules of use; OA articles are governed by the applicable Creative Commons License

A

	Detected	Quantified	Significantly altered	Differentially expressed
Proteome	9107	8595	991	179

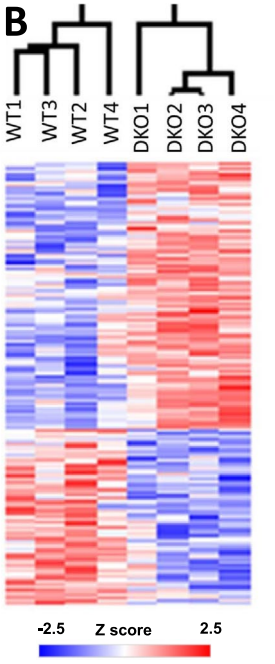

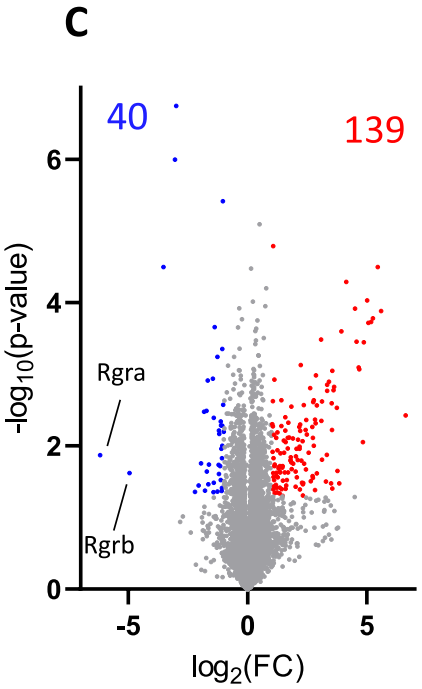

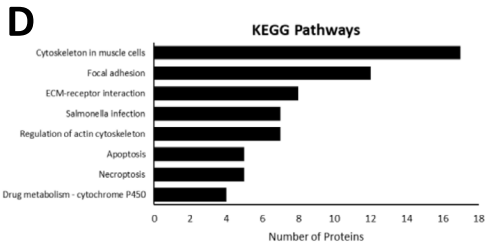

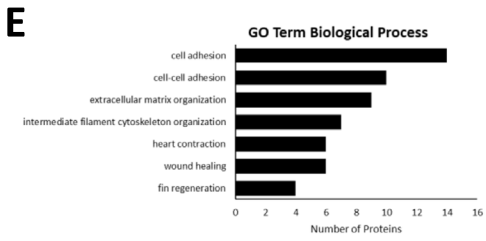

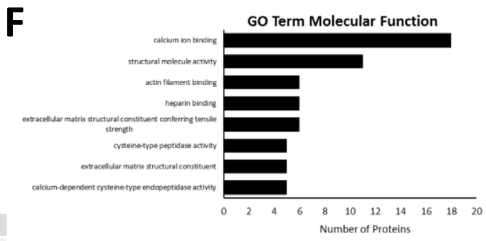

G Visual cycle

T-test p-value	Fold change	Protein Group	Genes	First Protein Description
0.953	-1.013	F1Q7T8	*lrata*	Lecithin retinol acyltransferase
0.433	1.089	B3DHX4	*lratb.2*	Lecithin retinol acyltransferase-like
0.029	1.383	A0A0R4IX64	*lratb.1*	Si:ch73-132f6.5
0.465	-1.109	STRA6	*stra6*	Receptor for retinol uptake stra6
0.001	-1.263	RP65A	*rpe65a*	Retinoid isomerohydrolase
0.380	1.534	RP65B	*rpe65b*	All-trans-retinyl ester 13-cis isomerohydrolase
0.091	2.225	RP65C	*rpe65c*	Retinal Mueller cells isomerohydrolase
0.372	-1.241	Q6PC74	*rlbp1a*	Cellular retinaldehyde-binding protein a
0.744	-1.042	Q6P027	*rlbp1b*	Cellular retinaldehyde-binding protein b
0.108	1.243	F1RCW4	*rdh5*	11-cis retinol dehydrogenase isoform X1
0.824	1.029	F1QT23	*rdh8b*	Retinol dehydrogenase 8b
0.739	1.066	Q6PC70	*rdh8a*	Retinol dehydrogenase 8
0.975	1.008	RD10A	*rdh10a*	Retinol dehydrogenase 10-A
0.704	1.055	Q6DG78	*rdh12*	Rdh12 protein
0.388	1.055	A0A8M1NAK9	*rdh14b*	Retinol dehydrogenase 14
0.896	1.046	Q5XJB5	*rdh14a*	Retinol dehydrogenase 14

H ECM structure and organisation

T-test p-value	Fold change	Protein Group	Genes	First Protein Description
0.009	3.03	A0A8M2BA28	*col11a1a*	Collagen alpha-1(XI) chain isoform X1
0.028	6.67	D6MUD3	*col11a1b*	Collagen alpha-1(XI) chain
0.049	4.99	A0A8M3AJ97	*col12a1a*	Collagen alpha-1(XII) chain isoform X1
0.023	3.23	A0A8M3AIZ5	*col14a1a*	Collagen alpha-1(XIV) chain isoform X1
0.050	2.77	L0S5L0	*col2a1b*	Collagen type II, alpha-1b
0.021	3.60	A0A8M9PD17	*col5a1*	Collagen alpha-1(V) chain isoform X1
0.033	4.88	A0A8M1NTE7	*col5a2a*	Collagen alpha-2(V) chain precursor
0.031	6.27	F1Q6P3	*col6a1*	Collagen alpha-1(VI) chain
0.032	9.71	A0A8M6Z0G5	*col6a3*	Uncharacterized protein col6a3 isoform X1
0.016	4.78	A0A8M3ATK9	*col7a1*	Collagen alpha-1(VII) chain isoform X1
0.022	13.66	Q7SYE5	*chad*	Chondroadherin
0.036	3.08	F1QL35	*thbs1b*	Thrombospondin 1b
0.012	2.90	A0A8M1RT39	*LOC100535166*	Thrombospondin-1-like
0.004	98.62	F1QSR3	*tnn*	Tenascin N
0.009	28.48	A0A0R4IS83	*postnb*	Periostin isoform X1
0.003	3.57	Q5BLF7	*itga6b*	Integrin, alpha 6b precursor
0.003	5.11	A0A8M2BEB1	*itgb4*	Integrin beta

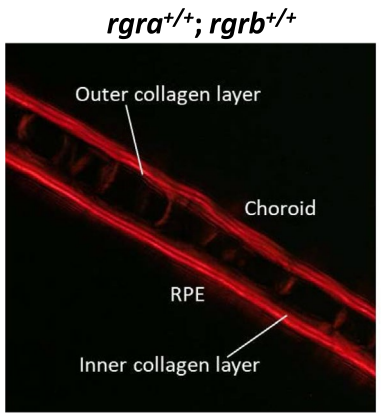

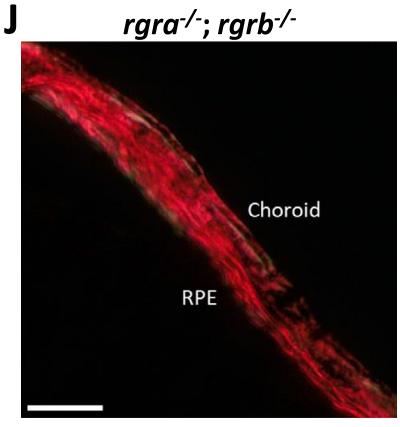

FIGURE 6 | Legend on next page.

15306860, 2026, 10, Downloaded from https://faseb.onlinelibrary.wiley.com/doi/10.1096/fj.202504935R by University Of California, Los Angeles, Wiley Online Library on [17/06/2026]. See the Terms and Conditions (https://onlinelibrary.wiley.com/terms-and-conditions) on Wiley Online Library for rules of use; OA articles are governed by the applicable Creative Commons License

FIGURE 6 | Loss of Rgra and Rgrb causes an upregulation of extracellular matrix (ECM) proteins and disrupted collagen fibril organization in Bruch's membrane. (A) Table summarizing the number of differentially expressed proteins detected in this experiment. (B) Heatmap demonstrating the clustering of differentially expressed proteins in WT and *rgrb*$^{-/-}$; *rgra*$^{-/-}$ zebrafish eyes. (C) Volcano plot depicting the proteins that are differentially expressed; upregulated (red) and downregulated (blue) between WT and *rgrb*$^{-/-}$; *rgra*$^{-/-}$ zebrafish. Rgra and Rgrb are highlighted. (D) Bar graphs listing the top KEGG Pathways identified by pathway enrichment analysis performed. (E) Bar graphs of the gene ontology analysis displaying the enriched *"Biological Process"* terms. (F) Bar graphs of the gene ontology analysis showing the enriched *"Molecular function"* terms. (G) List of identified visual cycle proteins (red = upregulated, blue = downregulated, gray = not changed). (H) List of ECM proteins that are upregulated in *rgrb*$^{-/-}$; *rgra*$^{-/-}$ zebrafish (red = upregulated). (I-J) Representative images of collagen fiber organization in the Bruch's membrane of WT (I) and *rgrb*$^{-/-}$; *rgra*$^{-/-}$ (J) adult zebrafish stained with PSR and imaged using polarized light microscopy. Red = collagen fibers. ($N = 3$, $n = 2$–3). Scale bar = 20 μm.

choroidal blood supply and the RPE, whose loss of integrity is associated with progression of IRDs and AMD.

Author Contributions

Grace Ruddin: conceptualization, data curation, formal analysis, funding acquisition, investigation, methodology, validation, visualization, writing – original draft preparation, writing – review and editing. **Tess McCann:** conceptualization, data curation, formal analysis, investigation, methodology, validation, visualization, writing – original draft preparation, writing – review and editing. **Joanna J. Kaylor:** data curation, formal analysis, investigation, methodology, validation, writing – review and editing. **Michelle M. Fox:** data curation, formal analysis, investigation, methodology, validation, visualization, writing – original draft preparation, writing – review and editing. **John D. Fehilly:** data curation, formal analysis, investigation, methodology, validation, writing – review and editing. **Rebecca Ward:** data curation, formal analysis, investigation, methodology, validation, writing – review and editing. **Adam Faulkner:** data curation, formal analysis, investigation, methodology, validation, writing – review and editing. **Ailís L. Moran:** data curation, formal analysis, investigation, methodology, validation, writing – review and editing. **Kieran Wynne:** data curation, formal analysis, investigation, methodology, validation, writing – review and editing. **Roxana A. Radu:** writing – review and editing. **Michael G. Monaghan:** conceptualization, data curation, methodology, resources, validation, writing – review and editing. **Stephen D. Thorpe:** conceptualization, data curation, methodology, resources, validation, writing – original draft preparation, writing – review and editing. **Gabriel H. Travis:** conceptualization, funding acquisition, methodology, writing – review and editing. **Breandán N. Kennedy:** conceptualization, data curation, formal analysis, funding. acquisition, methodology, project administration, resources, supervision, validation, visualization, writing – original draft preparation, writing – review and editing.

Acknowledgments

We would like to thank the UCD Conway Imaging Core (Dr. Niamh Stephens) and Genomics Core Facilities for technical expertise, the UCD BMF staff for zebrafish maintenance, and members of the UCD Ocular Pharmacology and Genetics Group for suggestions. We would like to thank Dr. Camilla Maria Fontana for her assistance with the light microscopy imaging. We would also like to thank Prof. Kenneth Wolfe and Prof. Geraldine Butler for their invaluable input with the phylogenetic analysis. Research reported in this publication was supported by The Comprehensive Molecular Analytical Platform (CMAP) under The SFI Research Infrastructure Programme, reference 18/RI/5702.

Funding

This publication was supported by research jointly funded by: Taighde Éireann—Research Ireland and Fighting Blindness under EPSPG/2023/1304 (GR), Taighde Éireann—Research Ireland under 20/FFP-P/8538 (BNK), The National University of Ireland (NUI) Traveling Studentship 2022 (JF), Irish Research Council/Fighting Blindness Grant EPSPG/2017/276 (RW) Irish Research Council grant EPS2019/526 (AM), UCD STEM Challenge Fund (BNK), NEI, National Institutes of Health (R01-EY024379) (G. H. T.) and Core Grant P30 EY00331 to the Jules Stein Eye Institute. Additional funding includes a Research to Prevent Blindness Stein Innovation Award (G. H. T.); and a Research to Prevent Blindness unrestricted grant to the Jules Stein Eye Institute. G. H. T. is the Charles Kenneth Feldman Professor of Ophthalmology at UCLA.

Conflicts of Interest

John D. Fehilly is a current employee of Eli Lilly and Company; this work was carried out prior to the start of employment.

Data Availability Statement

All data is contained in the figures and results section of the manuscript. The proteomic profiling data is available on request and will be available in an online repository pending publication.

References

1. K. Palczewski and P. D. Kiser, "Shedding New Light on the Generation of the Visual Chromophore," *Proceedings of the National Academy of Sciences of the United States of America* 117, no. 33 (2020): 19629–19638.

2. G. Ruddin, T. McCann, J. D. Fehilly, J. Kearney, and B. N. Kennedy, "The Dark and Bright Sides of Retinal G Protein-Coupled Receptor (RGR) in Vision and Disease," *Progress in Retinal and Eye Research* 106 (2025): 101339.

3. A. Terakita, "The Opsins," *Genome Biology* 6, no. 3 (2005): 213.

4. D. Shen, M. Jiang, W. Hao, L. Tao, M. Salazar, and H. K. Fong, "A Human Opsin-Related Gene That Encodes a Retinaldehyde-Binding Protein," *Biochemistry* 33, no. 44 (1994): 13117–13125.

5. L. Tao, D. Shen, S. Pandey, W. Hao, K. A. Rich, and H. K. Fong, "Structure and Developmental Expression of the Mouse RGR Opsin Gene," *Molecular Vision* 4 (1998): 25.

6. M. J. Bailey and V. M. Cassone, "Opsin Photoisomerases in the Chick Retina and Pineal Gland: Characterization, Localization, and Circadian Regulation," *Investigative Ophthalmology & Visual Science* 45, no. 3 (2004): 769–775.

7. W. I. L. Davies, T. K. Tamai, L. Zheng, et al., "An Extended Family of Novel Vertebrate Photopigments Is Widely Expressed and Displays a Diversity of Function," *Genome Research* 25, no. 11 (2015): 1666–1679.

8. B. A. Upton, N. M. Díaz, S. A. Gordon, R. N. Van Gelder, E. D. Buhr, and R. A. Lang, "Evolutionary Constraint on Visual and Nonvisual Mammalian Opsins," *Journal of Biological Rhythms* 36, no. 2 (2021): 109–126.

15306860, 2026, 10, Downloaded from https://faseb.onlinelibrary.wiley.com/doi/10.1096/fj.202504935R by University Of California, Los Angeles, Wiley Online Library on [17/06/2026]. See the Terms and Conditions (https://onlinelibrary.wiley.com/terms-and-conditions) on Wiley Online Library for rules of use; OA articles are governed by the applicable Creative Commons License

9. M. Jiang, S. Pandey, and H. K. Fong, "An Opsin Homologue in the Retina and Pigment Epithelium," *Investigative Ophthalmology & Visual Science* 34, no. 13 (1993): 3669–3678.

10. A. Morshedian, J. J. Kaylor, S. Y. Ng, et al., "Light-Driven Regeneration of Cone Visual Pigments Through a Mechanism Involving RGR Opsin in Müller Glial Cells," *Neuron* 102, no. 6 (2019): 1172–1183.e5.

11. J. Zhang, E. H. Choi, A. Tworak, et al., "Photic Generation of 11-Cis-Retinal in Bovine Retinal Pigment Epithelium," *Journal of Biological Chemistry* 294, no. 50 (2019): 19137–19154.

12. A. Tworak, A. V. Kolesnikov, J. D. Hong, et al., "Rapid RGR-Dependent Visual Pigment Recycling Is Mediated by the RPE and Specialized Müller Glia," *Cell Reports* 42, no. 8 (2023): 112982.

13. H. Morimura, F. Saindelle-Ribeaudeau, E. L. Berson, and T. P. Dryja, "Mutations in RGR, Encoding a Light-Sensitive Opsin Homologue, in Patients With Retinitis Pigmentosa," *Nature Genetics* 23, no. 4 (1999): 393–394.

14. R. Ba-Abbad, M. Leys, X. Wang, et al., "Clinical Features of a Retinopathy Associated With a Dominant Allele of the RGR Gene," *Investigative Ophthalmology & Visual Science* 59, no. 12 (2018): 4812–4820.

15. M. Jiang, D. Shen, L. Tao, S. Pandey, K. Heller, and H. K. Fong, "Alternative Splicing in Human Retinal mRNA Transcripts of an Opsin-Related Protein," *Experimental Eye Research* 60, no. 4 (1995): 401–406.

16. H. K. W. Fong, M. Y. Lin, and S. Pandey, "Exon-Skipping Variant of RGR Opsin in Human Retina and Pigment Epithelium," *Experimental Eye Research* 83, no. 1 (2006): 133–140.

17. M. Y. Lin, H. Kochounian, R. E. Moore, T. D. Lee, N. Rao, and H. K. W. Fong, "Deposition of Exon-Skipping Splice Isoform of Human Retinal G Protein-Coupled Receptor From Retinal Pigment Epithelium Into Bruch's Membrane," *Molecular Vision* 13 (2007): 1203–1214.

18. H. Kochounian, L. V. Johnson, and H. K. W. Fong, "Accumulation of Extracellular RGR-d in Bruch's Membrane and Close Association With Drusen at Intercapillary Regions," *Experimental Eye Research* 88, no. 6 (2009): 1129–1136.

19. W. Hao and H. K. Fong, "The Endogenous Chromophore of Retinal G Protein-Coupled Receptor Opsin From the Pigment Epithelium," *Journal of Biological Chemistry* 274, no. 10 (1999): 6085–6090.

20. P. Chen, W. Hao, L. Rife, et al., "A Photic Visual Cycle of Rhodopsin Regeneration Is Dependent on Rgr," *Nature Genetics* 28, no. 3 (2001): 256–260.

21. N. Morimoto, T. Nagata, and K. Inoue, "Reversible Photoreaction of a Retinal Photoisomerase," *Retinal G-Protein-Coupled Receptor RGR. Biochemistry* 62, no. 9 (2023): 1429–1432.

22. J. D. Hong, D. Salom, E. H. Choi, et al., "Retinylidene Chromophore Hydrolysis From Mammalian Visual and Non-Visual Opsins," *Journal of Biological Chemistry* 300, no. 3 (2024): 105678.

23. M. Yang, X. G. Wang, J. T. Stout, et al., "Expression of a Recombinant Human RGR Opsin in Lentivirus-Transduced Cultured Cells," *Molecular Vision* 18, no. 6 (2000): 237–242.

24. M. Yang and H. K. W. Fong, "Synthesis of the All-Trans-Retinal Chromophore of Retinal G Protein-Coupled Receptor Opsin in Cultured Pigment Epithelial Cells," *Journal of Biological Chemistry* 277, no. 5 (2002): 3318–3324.

25. R. A. Radu, J. Hu, J. Peng, D. Bok, N. L. Mata, and G. H. Travis, "Retinal Pigment Epithelium-Retinal G Protein Receptor-Opsin Mediates Light-Dependent Translocation of All-Trans-Retinyl Esters for Synthesis of Visual Chromophore in Retinal Pigment Epithelial Cells," *Journal of Biological Chemistry* 283, no. 28 (2008): 19730–19738.

26. R. Richardson, D. Tracey-White, A. Webster, and M. Moosajee, "The Zebrafish Eye-a Paradigm for Investigating Human Ocular Genetics," *Eye* 31, no. 1 (2017): 68–86.

27. S. E. Brockerhoff, J. B. Hurley, U. Janssen-Bienhold, S. C. Neuhauss, W. Driever, and J. E. Dowling, "A Behavioral Screen for Isolating Zebrafish Mutants With Visual System Defects," *Proceedings of the National Academy of Sciences of the United States of America* 92, no. 23 (1995): 10545–10549.

28. M. Gouy, S. Guindon, and O. Gascuel, "SeaView Version 4: A Multiplatform Graphical User Interface for Sequence Alignment and Phylogenetic Tree Building," *Molecular Biology and Evolution* 27, no. 2 (2010): 221–224.

29. F. Sievers, A. Wilm, D. Dineen, et al., "Fast, Scalable Generation of High-Quality Protein Multiple Sequence Alignments Using Clustal Omega," *Molecular Systems Biology* 7, no. 1 (2011): 539.

30. S. Guindon, J. F. Dufayard, V. Lefort, M. Anisimova, W. Hordijk, and O. Gascuel, "New Algorithms and Methods to Estimate Maximum-Likelihood Phylogenies: Assessing the Performance of PhyML 3.0," *Systematic Biology* 59, no. 3 (2010): 307–321.

31. A. Sur, Y. Wang, P. Capar, G. Margolin, and J. A. Farrell, "Single-Cell Analysis of Shared Signatures and Transcriptional Diversity During Zebrafish Development," *bioRxiv* 58, no. 24 (2023): 3028–3047, 533545, https://doi.org/10.1101/2023.03.20.533545.

32. T. Hoang, J. Wang, P. Boyd, et al., "Gene Regulatory Networks Controlling Vertebrate Retinal Regeneration," *Science* 370, no. 6519 (2020): eabb8598.

33. A. Gómez Sánchez, Y. Álvarez, B. Colligris, and B. N. Kennedy, "Affordable and Effective Optokinetic Response Methods to Assess Visual Acuity and Contrast Sensitivity in Larval to Juvenile Zebrafish," *Open Res Eur* 12, no. 1 (2021): 92.

34. J. D. Fehilly, T. McCann, G. Ruddin, et al., "Germline Disruption of Retinal Pigment Epithelium-Expressed Zebrafish rlbp1b-/- Results in Selective Dim Light Visual Behavior Deficits and Provides a Screening Platform for Evaluating the Pathogenicity of Human RLBP1 Variants," *FASEB Journal* 39, no. 12 (2025): e70754.

35. A. L. Moran, S. P. Carter, J. J. Kaylor, et al., "Dawn and Dusk Peaks of Outer Segment Phagocytosis, and Visual Cycle Function Require Rab28," *FASEB Journal* 36, no. 5 (2022): e22309.

36. C. Koenig, A. Martinez-Val, P. Naicker, S. Stoychev, J. Jordaan, and J. V. Olsen, "Protocol for High-Throughput Semi-Automated Label-Free- Or TMT-Based Phosphoproteome Profiling," *STAR Protocols* 4, no. 3 (2023): 102536.

37. N. Bache, P. E. Geyer, D. B. Bekker-Jensen, et al., "A Novel LC System Embeds Analytes in Pre-Formed Gradients for Rapid, Ultra-Robust Proteomics," *bioRxiv* 17, no. 11 (2018): 2284–2296, https://doi.org/10.1101/323048.

38. F. Meier, A. D. Brunner, S. Koch, et al., "Online Parallel Accumulation-Serial Fragmentation (PASEF) With a Novel Trapped Ion Mobility Mass Spectrometer," *Molecular & Cellular Proteomics* 17, no. 12 (2018): 2534–2545.

39. F. Meier, A. D. Brunner, M. Frank, et al., "diaPASEF: Parallel Accumulation-Serial Fragmentation Combined With Data-Independent Acquisition," *Nature Methods* 17, no. 12 (2020): 1229–1236.

40. V. Demichev, C. B. Messner, S. I. Vernardis, K. S. Lilley, and M. Ralser, "DIA-NN: Neural Networks and Interference Correction Enable Deep Proteome Coverage in High Throughput," *Nature Methods* 17, no. 1 (2020): 41–44.

41. S. Tyanova, T. Temu, P. Sinitcyn, et al., "The Perseus Computational Platform for Comprehensive Analysis of (Prote)omics Data," *Nature Methods* 13, no. 9 (2016): 731–740.

42. C. Greiner, S. Grainger, S. Farrow, et al., "Robust Quantitative Assessment of Collagen Fibers With Picrosirius Red Stain and Linearly Polarized Light as Demonstrated on Atherosclerotic Plaque Samples," *PLoS One* 16, no. 3 (2021): e0248068.

15306860, 2026, 10, Downloaded from https://faseb.onlinelibrary.wiley.com/doi/10.1096/fj.202504935R by University Of California, Los Angeles, Wiley Online Library on [17/06/2026]. See the Terms and Conditions (https://onlinelibrary.wiley.com/terms-and-conditions) on Wiley Online Library for rules of use; OA articles are governed by the applicable Creative Commons License

43. J. Schindelin, I. Arganda-Carreras, E. Frise, et al., "Fiji: An Open-Source Platform for Biological-Image Analysis," *Nature Methods* 9, no. 7 (2012): 676–682.

44. A. E. Sears and K. Palczewski, "Lecithin:Retinol Acyltransferase: A Key Enzyme Involved in the Retinoid (Visual) Cycle," *Biochemistry* 55, no. 22 (2016): 3082–3091.

45. L. Prieto-López, X. Pereiro, and E. Vecino, "The Mechanics of the Retina: Müller Glia Role on Retinal Extracellular Matrix and Modelling," *Front Med (Lausanne)* 4, no. 11 (2024): 1393057.

46. L. Fu, D. Garland, Z. Yang, et al., "The R345W Mutation in EFEMP1 Is Pathogenic and Causes AMD-Like Deposits in Mice," *Human Molecular Genetics* 16, no. 20 (2007): 2411–2422.

Supporting Information

Additional supporting information can be found online in the Supporting Information section. **Figure S1:** fsb271877-sup-0001-FigureS1.pdf. **Expression profile of zebrafish *rgra* and *rgrb* in whole larvae**. (A-C) Expression profile of zebrafish *rgra* and *rgrb* in whole zebrafish larvae generated from the online resource Daniocell https://daniocell.nichd.nih.gov/index.html. (A) UMAP projection of gene expression from whole 5 dpf zebrafish larvae. (B) Zebrafish *rgra* is predominantly expressed in the eye, glial, neural, spinal cord, mesenchyme and iridophores. (C) Zebrafish *rgrb* is predominantly expressed in the eye, glial, liver, mesenchyme, neural, iridophores, exocrine pancreas, xanthophores, pronephros and gut. The strongest expression is depicted by red patterning. **Figure S2:** fsb271877-sup-0002-FigureS2.pdf. **Collagen fiber quantification for WT and *rgrb*$^{-/-}$; *rgra*$^{-/-}$ zebrafish**. (A-B) CT-fire for fiber quantification for WT and *rgrb*$^{-/-}$; *rgra*$^{-/-}$ zebrafish. There was a significant difference in the collagen fiber count ($p = 0.0355$) between WT and *rgrb*$^{-/-}$; *rgra*$^{-/-}$ zebrafish (A) but not for the collagen fiber width ($p = 0.066$) (B). Graphs represent the mean ± SD, with each symbol representing a biological replicate. (WT: $N = 2$, $n = 3$–4, *rgrb*$^{-/-}$; *rgra*$^{-/-}$: $N = 3$, $n = 3$–4). Data was analyzed with a Welch's t test, and it passed the Shapiro–Wilk test. **Figure S3:** fsb271877-sup-0003-FigureS3.pdf. **Loss of Rgra and Rgrb disrupts the collagen fiber organization of Bruch's membrane, identified using SHG imaging**. (A-B) Representative images of collagen fiber organization in the Bruch's membrane of WT (A) and *rgrb*$^{-/-}$; *rgra*$^{-/-}$ (B) adult zebrafish using SHG microscopy. (A) Bruch's membrane of WT exhibits train-track-like architecture with lateral collagen fibrils bordering a collagen-free space. Feature width: 11–16 μm. (B) The collagen fibrils are disorganized and blended into irregular, rope-like bundles. Feature width: 14–18 μm. $N = 1$, $n = 1$. Scale bars: Overview 50 μm, inset: 20 μm. **Figure S4:** Top upregulated proteins in the *rgrb*$^{-/-}$; *rgra*$^{-/-}$ double knockout compared to WT. **Figure S5:** Top downregulated proteins in the *rgrb*$^{-/-}$; *rgra*$^{-/-}$ double knockout compared to WT.

15306860, 2026, 10, Downloaded from https://faseb.onlinelibrary.wiley.com/doi/10.1096/fj.202504935R by University Of California, Los Angeles, Wiley Online Library on [17/06/2026]. See the Terms and Conditions (https://onlinelibrary.wiley.com/terms-and-conditions) on Wiley Online Library for rules of use; OA articles are governed by the applicable Creative Commons License